Science of the Total Environment 1033 (2026) 181850

Contents lists available at ScienceDirect

Science of the Total Environment

journal homepage: www.elsevier.com/locate/scitotenv

Land subsidence dynamics in the Mekong Delta: Insights from local high-resolution geomechanical parameterization, numerical modelling, and geodetic observations

Felix Dörr [a,*], Jonas Bauer [a], Tran Viet Hoan [a,b], Le Thi Mai Van [b], Andreas Schenk [c], Nils Dörr [c], Franz Nestmann [d], Stefan Norra [e]

[a] Karlsruhe Institute of Technology (KIT), Institute of Applied Geosciences, Kaiserstraße 12, 76131, Karlsruhe, Germany
[b] National Center for Water Resources Planning and Investigation (NAWAPI), No. 93, lane 95, Vu Xuan Thieu Street, Sai Dong Ward, Long Bien District, Hanoi, 100000, Viet Nam
[c] Karlsruhe Institute of Technology (KIT), Institute of Photogrammetry and Remote Sensing, Kaiserstraße 12, 76131, Karlsruhe, Germany
[d] Karlsruhe Institute of Technology (KIT), Institute for Water and Environment, Kaiserstraße 12, 76131, Karlsruhe, Germany
[e] Potsdam University, Institute of Environmental Sciences and Geography, Soil Sciences and Geoecology, Campus Golm, Building 12, 14476, Potsdam Golm, Germany

HIGHLIGHTS

- Fully-coupled flow-deformation model used to simulate subsidence in Mekong Delta.
- The Mekong Delta will face delayed subsidence due to past groundwater depletion.
- Well-casing failure can accelerate land subsidence.

GRAPHICAL ABSTRACT

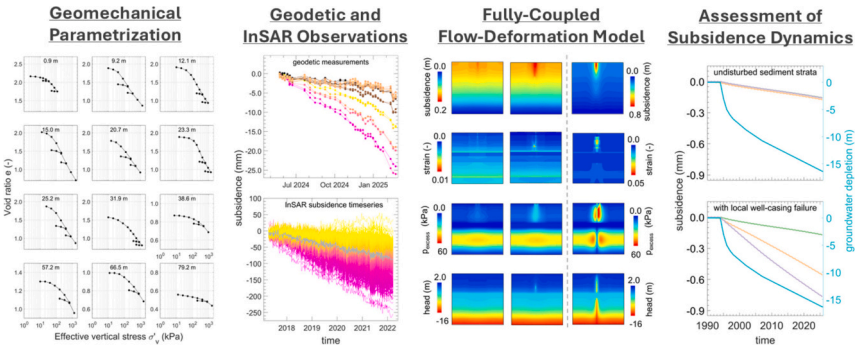

ARTICLE INFO

Keywords:
Land subsidence
Fully-coupled flow-deformation model
Mekong Delta
Groundwater overexploitation

ABSTRACT

Land subsidence poses major threats to human and environmental systems in river deltas worldwide, increasing risks of flooding and damage to civil infrastructure. In deltaic settings, land subsidence can be induced by multiple superimposing processes, including autocompaction, groundwater depletion and infrastructural surface loading. The quantification of each individual process is often uncertain, yet crucial for effective adaptation and mitigation. The Vietnamese Mekong Delta (VMD) is a prominent example of such a subsiding delta, with satellite-derived subsidence rates of up to 30 mm a^{-1} and surface elevations largely below 1 m above mean sea level. By presenting a fully coupled flow–deformation model with geomechanical parameterization at high vertical resolution, this study, supported by local geodetic leveling observations, provides an unprecedentedly detailed local-scale assessment of land subsidence dynamics for the VMD. The simulation results indicate subsidence rates of 5–6 mm a^{-1} due to groundwater depletion and local infrastructure loading. Additionally integrating one or

* Corresponding author.
E-mail address: felix.doerr@kit.edu (F. Dörr).

https://doi.org/10.1016/j.scitotenv.2026.181850
Received 5 January 2026; Received in revised form 25 April 2026; Accepted 30 April 2026
Available online 3 May 2026

multiple well-casing failures as localized subsurface disturbances in the model yields spatially heterogeneous subsidence patterns and increases local subsidence rates by an additional 1–20 mm a^{-1}, depending on the number of implemented failures. While well-casing failures are known consequences of land subsidence, the hypothesis-driven exploratory simulations employed here indicate that such damage may in turn accelerate subsidence by facilitating subsurface drainage pathways and local head equilibration between aquitards and tapped aquifers. This suggests that well-casing failures could contribute to heterogeneous and locally extreme subsidence dynamics. The results reveal significant delays in subsidence due to past groundwater depletion at the investigated site, underscoring the need for proactive water management strategies in the VMD, supported by comprehensive land subsidence modelling. The insights derived from this localized high-resolution analysis suggest that effective management will require preventing shallow aquifer depletion to avoid triggering the Holocene's pronounced, yet largely inactivated subsidence potential.

1. Introduction

Many of the world's coastal plains and river deltas are threatened by relative sea level rise, a combined effect of actual sea level rise due to global warming and land subsidence (Syvitski et al., 2009). While the actual sea level rise is in a range of approx. 3 mm a^{-1} on a global average, land subsidence rates can exceed these rates by 1–2 orders of magnitude (Davydzenka et al., 2024). This emphasizes the hazardous character of land subsidence and the urgent need for action in coastal settings. Consequences of land subsidence in delta systems range from increased exposure to flooding and seawater intrusion, loss of land and damages on civil infrastructure including bridges, roads and casings of water supply wells (Gambolati and Teatini, 2021; Holzer and Johnson, 1985).

The Vietnamese Mekong Delta (VMD) is a prominent example of a delta that is confronted with hazardous land subsidence rates. With an average surface elevation of approx. 0.8 m above mean sea level in 2018 (Minderhoud et al., 2019) and subsidence rates locally exceeding 30 mm a^{-1} (Erban et al., 2014; Dörr et al., 2024), these dynamics pose a substantial threat to the region's viability. In delta systems like the southern VMD, land subsidence can be induced by various superimposing processes including natural processes like autocompaction of shallow sediments (Zoccarato et al., 2018; Baldan et al., 2025), as well as anthropogenically triggered processes like sediment compaction due to groundwater extraction (Minderhoud et al., 2017, 2020). Furthermore, loading of civil infrastructure can additionally cause local sediment compaction below buildings and roads (Minderhoud et al., 2018).

Understanding the relative contributions of individual processes to total land subsidence is fundamental, as effective adaptation and mitigation strategies depend on identifying the governing mechanisms driving subsidence.

Most of the previous studies that aimed to quantify the contribution of either autocompaction or groundwater depletion to the overall subsidence are based on delta-wide numeric modelling (Baldan et al., 2025; Minderhoud et al., 2020, 2017; Zoccarato et al., 2018). These modelling approaches provided important first-order estimates and have significantly raised awareness of land subsidence in the Mekong Delta within both scientific and public communities. In light of the large size of the study area together with the high vertical and horizontal heterogeneity of the sediment strata, the limited availability of data for geomechanical parameterization represents an inherent challenge for large-scale subsidence models in the VMD.

In contrast to those delta-wide analyses, this study presents a local site-specific analysis, utilizing (i) InSAR and ground-based geodetic spatiotemporal subsidence observations, (ii) observed groundwater head data, and (iii) a detailed geomechanical subsurface parametrization based on incremental-loading oedometer tests on undisturbed drill-core samples for a fully-coupled flow-deformation simulation of land subsidence due to groundwater depletion and surface loading in the southern VMD.

This study elaborates numeric simulations for a process-based exploration of local land subsidence dynamics in an unprecedented level of detail for the southern VMD, providing new insights into process dynamics of land subsidence due to groundwater depletion and explores new potential factors for the spatiotemporal heterogeneity of observed subsidence rates. The analysis focuses on quantifying the contribution of various subsidence drivers at a non-urban research site with relatively high data density and explores additional mechanisms that may contribute to spatially heterogeneous subsidence rates in the immediate vicinity. In this context, the study proposes the hypothesis that well-casing failures, i.e. cracks and ruptures in the casing material, represent a previously unexplored mechanism potentially contributing to locally extreme and spatially heterogeneous subsidence rates in addition to those induced by groundwater depletion, surface loading, autocompaction and heterogeneous sediment characteristics. Such well-casing failures, long known consequences of land subsidence induced by groundwater depletion (Gambolati and Teatini, 2021; Holzer and Johnson, 1985), may additionally accelerate subsidence by facilitating subsurface drainage pathways and enabling local hydraulic head equilibration between aquitards and tapped aquifers.

2. Materials and methods

2.1. Hydrogeology and groundwater depletion

The VMD is characterized by a complex hydrogeological stratigraphy, which is commonly conceptualized as a multi-layered aquifer-aquitard system comprising seven aquifers and seven aquitards (Hoan et al., 2022, Fig. 1c). In the southern VMD, the topmost Holocene aquifer *qh* is not continuously developed (Dörr et al., 2026) and the clay-silt sequences of the Holocene and Pleistocene aquitards Q_2 and Q_1^3 can merge, forming a single aquitard above the upper Pleistocene aquifer qp_3. In Ca Mau Province, the southernmost province of the southern VMD, the Holocene-Pleistocene interface is located at a depth of approx. 20 m (Mi et al., 2023). In this region, the qp_3 aquifer is the first continuously developed aquifer, yet it is rarely utilized for groundwater extraction (Hoan et al., 2022). The highest groundwater extraction rates have been reported for the upper-middle Pleistocene aquifer qp_{2-3} (Hoan et al., 2022), whereas more recently deeper aquifers like the middle Pliocene aquifer n_2^2 are subject to increasing exploitation due to salinization processes in the upper aquifers (Hoan et al., 2025).

Prior to significant anthropogenic groundwater extraction, early studies documented artesian groundwater heads in the southern VMD (Anderson, 1978). Since 1995, groundwater head measurements provided by the Vietnamese National Groundwater Monitoring Network (NGMN) have documented a continuous decline in groundwater heads over the past three decades. At the study site GW1 (Fig. 1b), groundwater heads have been monitored since 2022 in several aquifers, including an observation well (GW1a) screened in the upper–middle Pleistocene aquifer (qp_{2-3}), and, temporarily between May and August 2024, in an observation well (GW1d) screened in the upper Pleistocene aquifer (qp_3). The monitoring site GW1, located in Ca Mau Province, was established in collaboration of the Karlsruhe Institute of Technology (KIT), the National Center for Water Resources Planning and Investigation (NAWAPI) and the Department of Natural Resources and Environment Ca Mau (DONRE Ca Mau) as part of the German-Vietnamese

ViWaT-Engineering research project funded by the Vietnamese Ministry of Natural Resources and Environment and the German Ministry of Research, Technology and Space.

Fig. 1a illustrates groundwater head data for the monitoring site Q177 in Ca Mau city for the period 1995 until 2025 as well as for the monitoring site GW1 from 2022 until 2025, respectively. It is noted that despite its attribution to the Holocene aquifer *qh* in the NGMN database and in previous studies (e.g. Van et al., 2023), the monitoring well Q17701T is not screened in Holocene aquifer *qh*. A review of the respective drilling profile (see supplementary information S3) indicates that this observation well is screened in 2.5–8.5 m depth, clearly within the Holocene aquitard Q_2. Therefore, the stagnant trend with seasonal variations in the observation data cannot be interpreted as hydraulic head but rather as an indicator for constant saturation in the top of the Holocene aquitard Q_2 and an influence of seasonal surface water loading.

The seasonal rise in groundwater heads at GW1 (Fig. 1a) was identified to be due to surface loading effects, driven by a seasonal accumulation of water resources in the surrounding aquaculture ponds (Dörr et al., 2026). A removal of these loading effects for the rainy season 2023 revealed a continuous groundwater depletion in qp_{2-3} (Dörr et al., 2026). For the employed numeric simulation of sediment compaction at GW1, annual average, therefore loading independent, groundwater head depletion rates are utilized. For the model implementation, hydraulic head boundary conditions are derived from locally observed groundwater heads at GW1 between 2022 and 2025, while earlier depletion trends between 1995 and 2022 are approximated based on groundwater head trends at Q177 (dashed lines in Fig. 1a).

2.2. Subsurface characterization

The geomechanical subsurface parametrization for GW1 is derived from a total number of twelve one-dimensional compression tests using undisturbed drill core samples from distinct depths between 0.9 m and 79.2 m, obtained from the drilling of the observation well GW1c in the southern VMD. For each sample, the compression index C_c (−) and the recompression index C_r (−) are derived from the slopes of the linearized sections in the obtained compressibility curves. From the time-compression curve at the load stage representative for the in-situ pressure conditions, the coefficient of secondary (creep) compression C_α (−) and the coefficient of consolidation c_v ($m^2\ s^{-1}$) as well as the vertical hydraulic conductivity k_v ($m\ s^{-1}$) are calculated. C_α is derived from the gradient of the linearized section in the obtained semilogarithmic time-compression curve. c_v is calculated with the *Casagrande Logarithm of Time Fitting Method* by Eq. (1) to

$$c_v = 0,196 \cdot \frac{(h/2)^2}{t_{50}} \tag{1}$$

where h (m) is the sample's height and t_{50} (s) is the time at 50% of primary consolidation. k_v is calculated with Eq. (2), where γ_w is the unit weight of water (~ 10 kN m^{-3}) and m_v (kPa $^{-1}$) is the coefficient of volume compressibility, which is derived with Eq. (3), where $\Delta\sigma'_{v,i}$ (kPa) is the vertical effective stress increment at the loading step i, Δe_i (−) is the change of void ratio during the loading step i and e_{i-1} (−) is the void ratio in the previous loading step.

$$k_v = c_v m_v \gamma_w \tag{2}$$

$$m_{v,i} = \frac{\Delta e_i}{\Delta\sigma'_{v,i}(1 + e_{i-1})} \tag{3}$$

The preconsolidation stress σ'_p (kPa) is derived from the experimental data with the opensource software tool *pySigmaP* (Montoya-Araque et al., 2022), which incorporates several established methods e.g. the approaches of *Casagrande*, *Pacheco Silva* and *Boone*. The method of Boone provides an alternative to the historically established methods of Casagrande and Pacheco Silva, aiming to overcome uncertainties due to the graphical approximations used in those methods. The method of Boone takes the in-situ effective vertical stress σ'_{v0} (kPa) as well as C_c (−) and C_r (−) into account and was used to derive σ'_p in this study. From σ'_p and σ'_{v0} the overconsolidation ratio *OCR* (−) is calculated to

$$OCR = \frac{\sigma'_p}{\sigma'_{v0}} \tag{4}$$

For each sample, the void ratio e (−) and the unit weight γ (kN m^{-3}) were determined based on weighing the undisturbed and dried sample.

To characterize the soil's properties under unsaturated conditions,

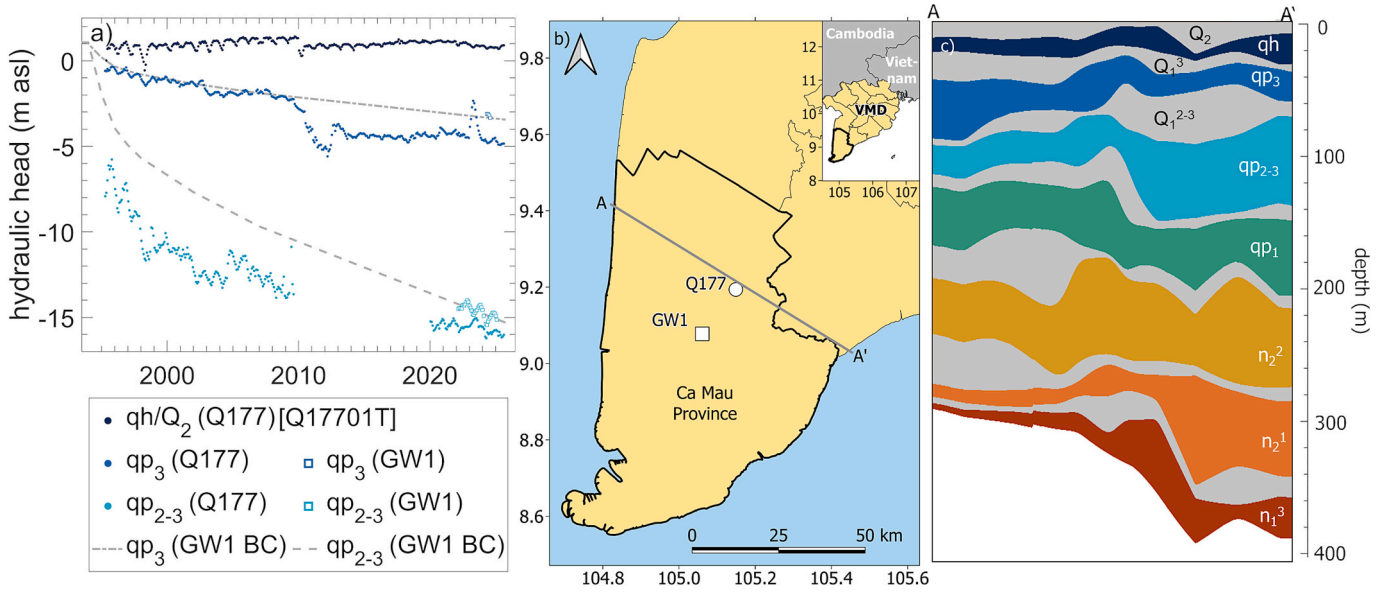

Fig. 1. Hydraulic head observations from the monitoring site Q177 in Ca Mau city from 1995 until 2025 and from the monitoring site GW1 between 2022 and 2025, in the aquifers qp_{2-3} and qp_3, respectively. Additionally, observation data from the observation well Q17701T screened in the Holocene aquitard at the monitoring site Q177 is included, denoted as qh / Q_2. Data displayed as monthly mean values (a). Map of the study area in the southern VMD including the locations of the monitoring sites GW1 and Q177 (b) and hydrogeological cross-section (Hoan et al., 2022) with aquifers in colors and aquitards in gray (c).

the soil water characteristic curves (SWCC) are derived for GW1 in five depths between 0.3 m and 1.0 m. For that, undisturbed soil samples were analyzed in the laboratory by measuring the volumetric water content θ (−) and the corresponding matric potential Ψ (kPa). Based on the measurement data, the Van Genuchten parameters α (kPa^{-1}) and n (−) are derived, providing a mathematical representation of the SWCC. Additionally, the grain size distribution is analyzed for seven samples at depths between 0.1 m and 1.0 m. The obtained soil classes are used to compare the calculated values for α and n with standard literature values for specific soil and sediment classes (Tuller and Or, 2005).

2.3. Leveling and InSAR monitoring

Between May 22, 2024, and February 23, 2025, a total of 35 geodetic monitoring campaigns were carried out in the vicinity of GW1. Each campaign comprised (i) 13 measurement points located at the GW1 site, (ii) one monitoring point positioned on the pile foundation of a nearby bridge, and (iii) six additional points situated between the bridge and GW1, adjacent to the road and neighboring urban dwellings. The location of the monitoring points is visualized in the supplementary information S2 and in the presented results. The leveling results are referenced to the monitoring point located on the bridge foundation, assuming the bridge's deep piled foundation to be stable and unaffected by Holocene and shallow Pleistocene compaction. This approach is generally consistent with that of Dörr et al. (2024), who used bridge foundations as reference networks for InSAR analyses in the southern VMD, with estimated foundation depths of approximately 70 m. The geodetic leveling was conducted in closed loops, allowing for assessment of the vertical misclosure. The median misclosure in the 35 geodetic monitoring campaigns is low with 0.29 mm and presented in detail in the supplementary information S1.

The geodetic monitoring network at GW1 comprises the points PW3–PW8 on the well head and pedestal of the three observation wells (GW1a, GW1b, and GW1c), points CR10–CR14 on the pedestal and metal plates of the corner reflector, and points PW1–PW2 on the well head and pedestal of the sliding-joint-based multi-extensometer drilling. The location of geodetic monitoring points on the site GW1 is illustrated in the supplementary information S2. The points P102–P105 are located within one to three meters of the road lane and thus are presumably still positioned on the road embankment. The points P100 and P101 are located in a driveway and within a sealed courtyard.

To contextualize the geodetic leveling results, these observations from 2024 to 2025 are compared with InSAR-derived subsidence time series of persistent scatterers in the vicinity of GW1, extracted from a dataset covering the period 2017–2022 (Dörr et al., 2024). Although the time series do not overlap, and the exact locations of the geodetic points are not resembled in the InSAR data, similarities in trends, spatial heterogeneity, and seasonal patterns allow for a qualitative assessment of consistency and plausibility.

2.4. Subsidence model

In the present study, a fully coupled flow-deformation model is employed to simulate subsurface deformation and resulting land subsidence due to depleting groundwater heads at the monitoring site GW1 in the southern VMD. Within this framework, groundwater flow and mechanical deformation are solved simultaneously, allowing changes in effective stress and deformation to dynamically influence flow and hydraulic properties such as porosity and permeability, and vice versa. For this, the finite-element based commercial software tool *PLAXIS 2D* is used, utilizing the *SoftSoilCreep* model (Vermeer and Neher, 1999), which is an advanced geomechanical constitutive model.

The *SoftSoilCreep* model is capable of simulating time-dependent processes of consolidation and creep and was applied in previous studies to simulate settlement processes due to surface loading and groundwater level variations (Lee et al., 2018; Feng et al., 2019). Considering such time-dependent processes is essential, given that delayed compression of soils and sediments such as creep is a well-recognized process contributing to land subsidence (Qi et al., 2025), although creep is neglected in many studies on groundwater-depletion-induced subsidence (Kooi and Erkens, 2020).

The effects of saturation on the subsurface stresses are integrated in the PLAXIS implementation with the *Bishop stress formulation*

$$\boldsymbol{\sigma} = \boldsymbol{\sigma}' + \boldsymbol{m}(\chi p_w + (1-\chi)p_a) \quad (5)$$

where σ (kPa) is the tensor of total stresses, σ' (kPa) is the effective stress tensor, m is a tensor with unity terms for normal stress components and zero terms for the shear stress, χ (−) is the matric suction coefficient p_w (kPa) and p_a (kPa) are the pore water pressure and the pore air pressure (Galavi, 2010). In PLAXIS, the matric suction coefficient is internally calculated from the effective saturation, which is governed by the soil water characteristic curve model, here the Van Genuchten model and its corresponding parameters (Galavi, 2010). Additionally, the model considers a reduction of the hydraulic conductivity with advancing consolidation by the permeability change index C_k (−) which is estimated to $C_k \cong 0.5\, e_0$ (Tavenas et al., 1983). The model parameters are derived from the geomechanical characterization described above.

The 2D cross-sectional model developed in this study encompasses a lateral extent of 500 m and a vertical extent of 81 m (Fig. 2). The bottom of the model domain equals the interface between the middle Pleistocene aquitard Q_1^{2-3} and the highly exploited upper-middle Pleistocene aquifer qp_{2-3}. Therefore, the groundwater depletion in qp_{2-3} represents a model boundary condition, which is implemented by a transient Dirichlet boundary condition with a depletion rate derived from recent local and historic regional groundwater head data (Fig. 1a). The vertical model discretization covers 13 layers and was derived from sampling depths and sediment classifications. The finite-element mesh discretization includes 45,192 nodes and 22,275 triangular elements. The intermediate aquifer qp_3 is implemented in the model by a linear-elastic constitutive model. Similar to qp_{2-3}, the groundwater depletion in qp_3 is implemented by a transient Dirichlet boundary condition with a depletion rate derived from recent local and historic regional groundwater head data (Fig. 1a). This boundary condition is realized in the model on the aquifer's lateral boundary. The aquifer's hydraulic conductivity, which is of secondary importance for the simulated subsidence response compared to the locally derived aquitard deformation parameters, was determined to $3.2{\cdot}10^{-4}$ m s^{-1} based on regional aquifer parametrization and a calibrated groundwater flow model (Hoan et al., 2022). For the aquitards, an anisotropy ratio of hydraulic conductivity (k_h/k_v) of 3 was adopted, consistent with the parametrization in a recent study on Holocene sediments in the VMD by Baldan et al. (2025).

By covering a variety of land use and land cover (LULC) types including aquaculture, vegetation, road infrastructure and urban settlements adjacent to the road, the model comprises a typical representation of surface characteristics in the southern VMD. These various LULC types locally influence the hydraulic interaction between surface water resources and subsurface sediments and are hence differentiated in the assignment of hydraulic boundary conditions in the model. The road near GW1, QL1, is a historically used route, with an estimated age of up to 200 years and underwent several upgrades during colonial history (Logan, 2002). Assuming intermediate road rehabilitation to have negligible impact on the road's self-weight loading, consolidation processes related to the road construction itself are considered completed in this study. Sealed surfaces of roads and urban settlements locally prevent infiltration or rewetting processes and are therefore implemented in the model by no-flow Neumann boundary conditions, a reasonable consideration if the sediment strata is topped by a completely impermeable layer (Baú et al., 2004). For the spatially extensive aquaculture ponds however, which are commonly not lined with plastic foil, the ponds' water levels maintain the hydraulic conditions on the surface and can therefore be represented by a constant or transient Dirichlet

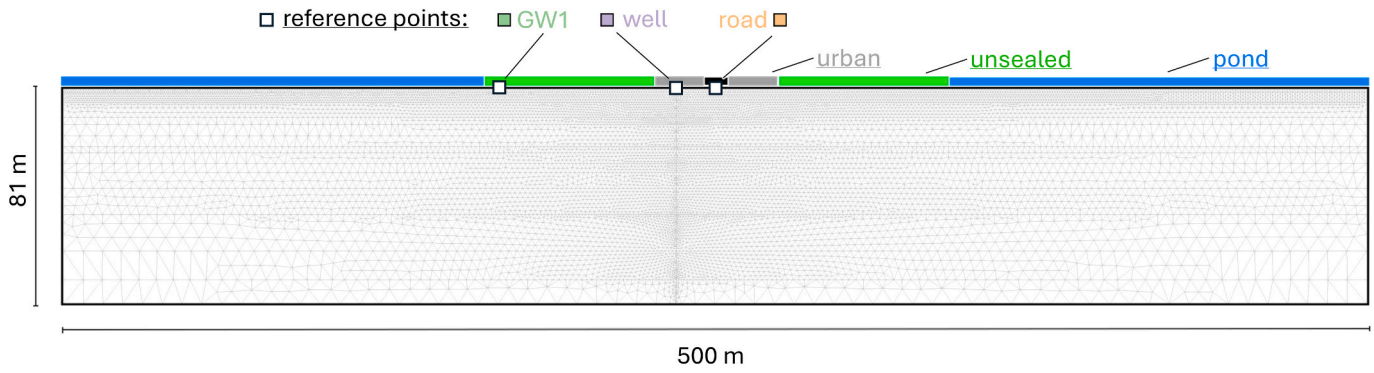

Fig. 2. 2-D Model domain illustrating the mesh and the spatial extent of surface boundary conditions for urban (gray), unsealed (green) and ponded (blue) surfaces as well as the road (black) in the center. Reference points for the site GW1, the urban well and the road which are used later on for the evaluation of computed subsidence time series are included.

boundary condition, e.g. as applied in analytical calculations by Gambolati and Teatini (2021). To account for the seasonal loading effects due to variations of surface water levels in aquaculture ponds near GW1, the Dirichlet boundary condition for aquaculture ponds are implemented as sinusoidally harmonic head variations with an annual oscillation period and an amplitude of 0.5 m. Such seasonal water level variations comply well with seasonal water level variations in aquaculture ponds in the study area (Dörr et al., 2026).

Vegetated surfaces, as well as a 1-m wide drainage channel situated on either side of the road, are implemented in the model by seepage boundary conditions. Such seepage boundary conditions locally permit water flow and therefore the dissipation of excess pore pressure toward the surface. On the road, a vehicle load of 10 kPa is applied according to Vietnamese standards referenced by Mi et al. (2023). Loads of buildings are not included in the calculations. To provide a contextualization of this consideration, the local loading of the predominantly one-story residential buildings is estimated to be within the range of the applied vehicle load (Xu et al., 2025).

It should be noted that the implemented surface load does not aim to accurately represent the actual loading conditions in the vicinity of GW1, but rather to capture a representative order of magnitude of typical urban surface loading in the VMD. By assuming design vehicle loads to be constant and neglecting the loading from residential buildings, this simplified representation of urban loading is considered reasonable within the context of this study.

To evaluate the hypothesis that damaged well casings may affect the spatiotemporal dynamics of land subsidence due to groundwater depletion, damaged casing segments of an exemplary well are implemented in the model by drainage boundary conditions within exploratory scenario simulations. Two main scenarios are considered: (i) a single well-casing failure located at depths of highest subsurface strain, and (ii) multiple failures implemented at regular intervals along the casing. In the latter case, damaged casing segments are introduced at intervals of 3 m, representing the typical length of casing pipe segments and failures at their interconnecting joints. In the main scenarios, individual failures are represented by 0.1 m long damaged casing segments. In addition, a sensitivity analysis is conducted to evaluate the influence of both the number of failures and the assumed failure length, reducing the latter from 0.1 m in the main scenarios to 0.05 m and 0.01 m in additional comparison simulations. At the drain boundary conditions, water outflow from the model is permitted and controlled by a specified reference head. The reference head of these drain boundaries corresponds to the water level within the well casing, and thus to the hydraulic head in the tapped aquifer. Since PLAXIS does not allow a fully dynamic implementation of reference heads in drain boundary conditions, they were incorporated into the model as annually constant values, discretely representing the depletion of the tapped aquifer as illustrated in the supplementary information S4. This approximation leads to a small offset relative to the hydraulic heads that would correspond to the casing water levels under the applied modelling concept, and therefore to a slight overestimation of the hydraulic head gradients and drainage. Moreover, this approach does not capture short-term fluctuations in hydraulic heads and casing water levels. Such variations have been shown to result predominantly from surface loading effects at GW1 (Dörr et al., 2026), which induce transient pressure responses in the aquifer system and can influence drainage dynamics.

Fig. 2 visualizes the model domain, including the variety of implemented surface boundary conditions for urban, unsealed and ponded surfaces and the finite element mesh, which is characterized by grid refinement close to the surface and near the implemented well casing.

In the *SoftSoilCreep* model, the initial creep deformation is overestimated if sediments are parametrized as ideally normally consolidated sediments (OCR = 1.0), as this would imply that the sediments have experienced their complete primary loading, i.e. the self-weight of any overlying sediment layers, within the preceding 24-h period prior to the start of the simulation. This is unrealistic in the context of geological formation history, where in most depths, the sediment strata have experienced loading for thousands of years already. To avoid such overestimated initial creep deformations to bias the calculation results, a 100,000-year period with constant hydraulic and geomechanical conditions is included in the simulation, prior to the calculation of compaction due to groundwater depletion and surface loading. To verify that the initial creep deformation reached insignificance, the simulated deformation rate prior to evaluation period starting from 1990 was checked to be <0.01 mm a^{-1}.

During the fully-coupled simulation, initially defined state variables like the void ratio as well as related parameters like the hydraulic conductivity change dynamically over the course of the simulation period. Since the model parameters were derived from samples collected in 2020, the initial parameterization was iteratively adjusted to ensure consistency with the 2020 reference state in the model.

3. Results

3.1. Observed subsidence rates

The observed land subsidence rates measured with ground-based leveling between May 2024 and February 2025 are characterized by a distinct spatial heterogeneity with higher subsidence rates near the road and adjacent urban settlements and lower subsidence rates at GW1 (Fig. 3a). The subsidence rates show temporal variations, with higher subsidence rates observed during the dry-season surveys (Fig. 3a-b), when groundwater heads and surface water levels decline. The greatest subsidence rates are measured at P101 with a subsidence rate of 50 mm a^{-1} in the dry season and 25 mm a^{-1} in the rainy season (Fig. 3b). At GW1, eleven of the thirteen subsidence observation points show very

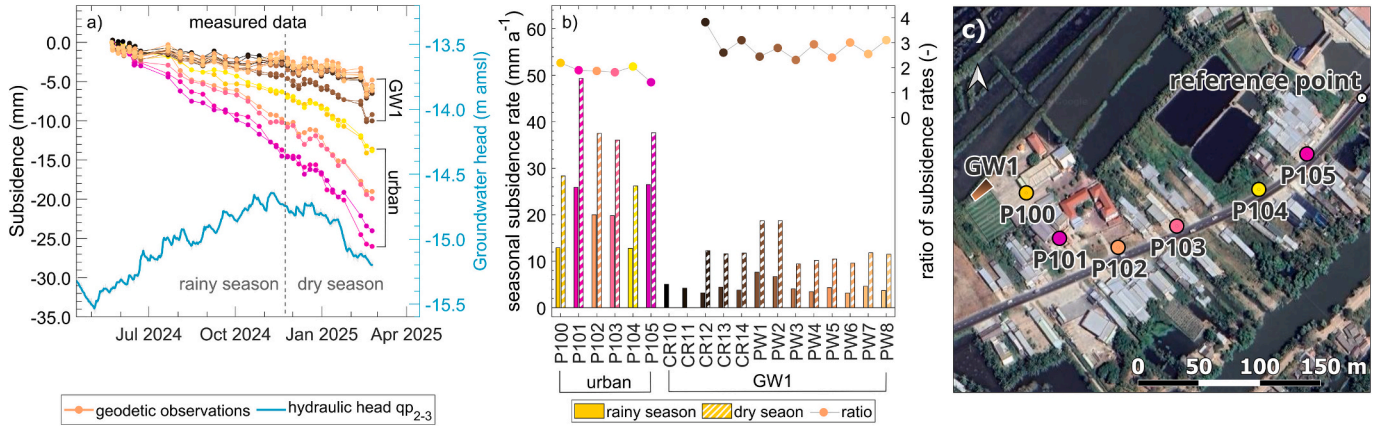

Fig. 3. Measured land subsidence rates and observed groundwater heads at GW1 (a), seasonal trends and ratio between dry season and rainy season subsidence (b), and location of subsidence observation points (c). In (c), individual measurement locations are omitted and only the spatial extent of monitoring site GW1 is shown; see Supplementary Information S2 for detailed locations.

similar dynamics (Fig. 3a), with an annual-average subsidence rate of 8 mm a^{-1} and trends between approx. 10 mm a^{-1} in the dry season and approx. 3 mm a^{-1} in the rainy season (Fig. 3b). Only the points PW1 and PW2, located at the well head and pedestal of the sliding-joint multi-extensometer drilling, show increased subsidence rates of approx. 13 mm a^{-1} and seasonal trends between approx. 18 mm a^{-1} in the dry season and approx. 8 mm a^{-1} in the rainy season (Fig. 3a-b).

Fig. 4 presents the InSAR-based subsidence observation in the vicinity of GW1, comprising (i) all individual subsidence time series and their average (Fig. 4a), (ii) a statistical summary of the corresponding subsidence rate distribution (Fig. 4b), (iii) a smoothed subsidence time series obtained from a 60-day moving-mean window of the averaged subsidence time series of all InSAR points (Fig. 4c), and (iv) a map showing the spatial distribution of the InSAR scatterers (Fig. 4d), color-coded in accordance with Fig. 4a-b). The subsidence dynamics are characterized by a pronounced variability (Fig. 4a-b) with a median subsidence rate of 15.7 mm a^{-1} (Fig. 4b). The averaged and smoothed subsidence time series reveals seasonal patterns with temporal rebound phases (Fig. 4c).

In the vicinity of GW1, 89% of the InSAR-derived scatterers (Fig. 4b) exhibited subsidence rates between 2017 and 2022 that exceeded the geodetically measured annual-average depletion rate of 8 mm a^{-1} at GW1 in 2024–2025.

3.2. Geomechanical subsurface characterization

The compression and recompression indices are derived from the compressibility curves of the one-dimensional compression tests for twelve distinct depths between 0.9 m and 79.2 m (Fig. 5). The results are summarized in depth profiles (Fig. 7) and show a high compressibility in the Holocene aquitard Q_2 and the upper Pleistocene aquitard Q_1^3 with compression indices between 0.59 and 1.06 (Fig. 7e) and a mean value of 0.77. The middle Pleistocene aquitard Q_1^{2-3} is characterized by distinctly lower compression indices between 0.21 and 0.46 (Fig. 7e). Similarly, the recompression indices are greater in Q_2 and Q_1^3 with values between 0.04 and 0.09, whereas in Q_1^{2-3} C_r varies between 0.02 and 0.07 (Fig. 7f). The ratio of C_c and C_r varies between 9.0 and 15.8 in Q_2 and Q_1^3. Fig. 5l shows that for the sample at 79.2 m depth, the maximum applied load of 1600 kPa, limited by the load capacity of the used oedometer apparatus, was possibly insufficient to clearly define the slope of the linear portion of the compressibility curve, thereby introducing uncertainty to the derived C_c value.

The compressibility curves of some samples (Fig. 5 b, d, f) show a lower gradient at higher stress stages after the linear trend in the semilogarithmic e- σ'_v plot. Such trends in compressibility curves have been observed for sensitive clays and are attributed to a greater degree of particle interaction and stronger resistance to structure compression (Boone, 2010). This aligns with previous findings (Giao et al., 2008), characterizing the soft clay sediments in Ca Mau as medium to very sensitive clay.

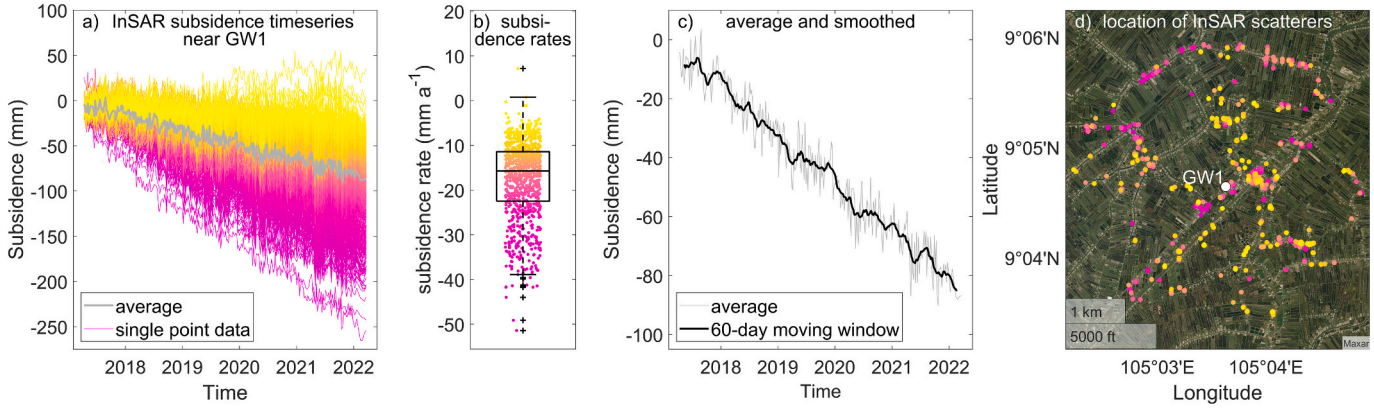

Fig. 4. InSAR-derived subsidence dynamics between 2017 and 2022 near GW1, comprising all individual time series and average (a), a distribution of annual subsidence rates (b), a 60-day moving-mean smoothed subsidence time series (c) and a spatial distribution of the InSAR scatterers (d). Note that the color scale in (d) is identical to that in (a) and (b), indicating observed subsidence magnitudes from low (yellow) to high (magenta).

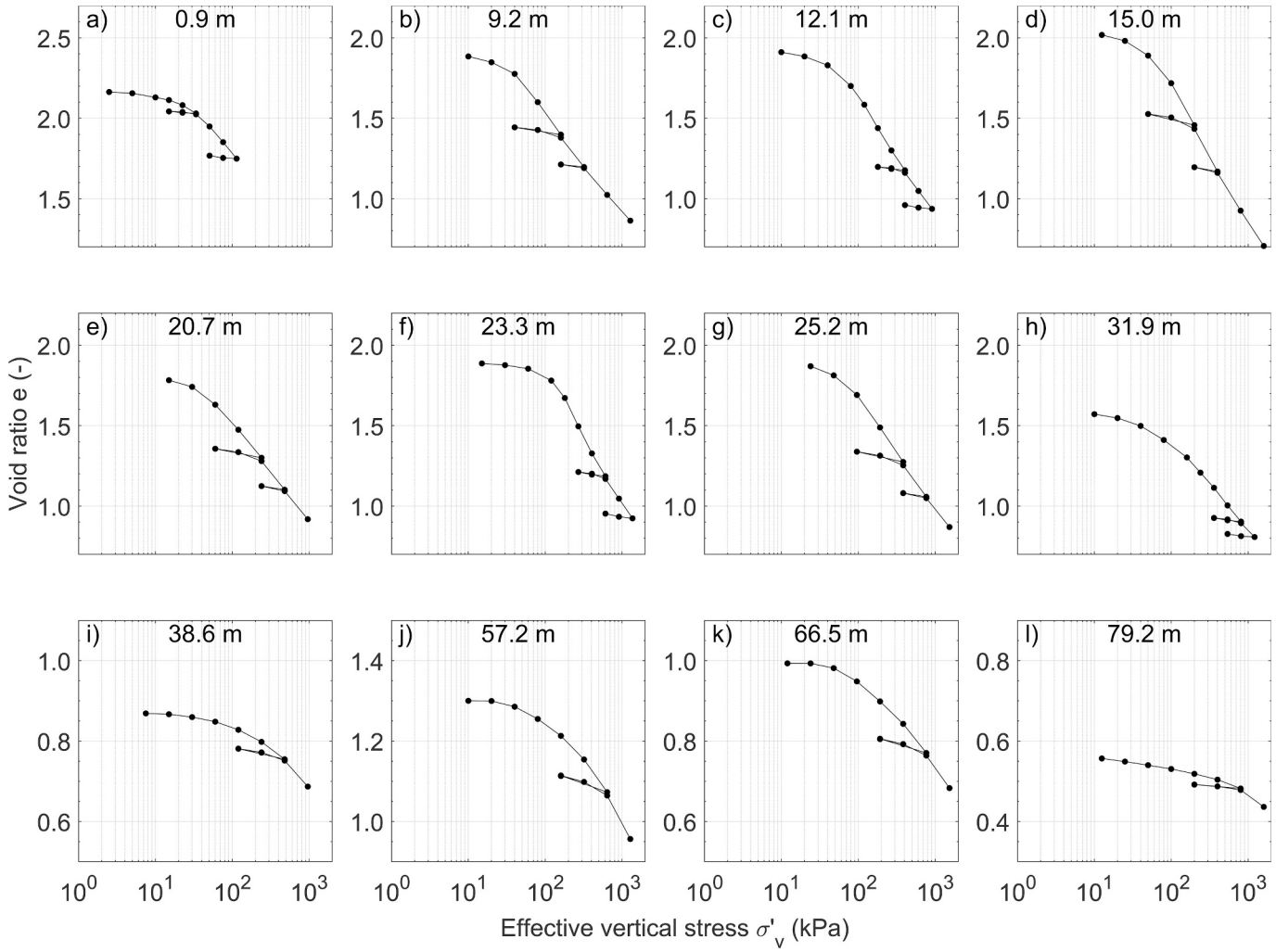

Fig. 5. Compressibility curves from twelve one-dimensional compression tests on undisturbed drill core samples from GW1 between 0.9 m and 79.2 m depth.

The secondary (creep) compression C_α (−) is derived from the time compression curves of the one-dimensional compression tests at a load stage representative for the in-situ effective stress at the corresponding depth. In Fig. 6, the twelve time-compression curves used for the calculation of C_α are summarized. Each time-compression curve is characterized by a distinct linear trend in the semilogarithmic plot, from which C_α is derived.

In Fig. 7, the obtained parameters for GW1 are visualized in profiles. This includes profiles of the samples' void ratio e (Fig. 7c) and unit weight γ (Fig. 7d), the compression index C_c (Fig. 7e), the recompression index C_r (Fig. 7f), the creep compression index C_α (Fig. 7g), the over-consolidation ratio OCR (Fig. 7h), the coefficient of consolidation c_v (Fig. 7i) and the vertical hydraulic conductivity k_v (Fig. 7j). In Fig. 7a, the sediment characterization is presented in form of a grain size distribution estimation based on an on-site evaluation of the drill cores during drilling. Based on the sediment characterization and the parameterization, a stratigraphic classification is derived and illustrated in Fig. 7b.

Except for the topmost sample (0.9 m depth) the overconsolidation ratio implies normally consolidated conditions in the Holocene aquitard Q_2 and the upper Pleistocene aquitard Q_1^3, with ranges of OCR between 1.04 and 1.19. In 0.9 m depth, OCR = 5.3 implies overconsolidated sediments in the topmost strata. The coefficient of consolidation varies between 1.2 $\cdot 10^{-8}$ and 5.4 $\cdot 10^{-8}$ $m^2\ s^{-1}$ in Q_2 and Q_1^3 and between 5.3 $\cdot 10^{-8}$ and 9.6 $\cdot 10^{-7}$ $m^2\ s^{-1}$ in Q_1^{2-3} (Fig. 7i).

Overall, the geomechanical characterization presented in Fig. 7 reveals a clear differentiation between the upper aquitard (comprising Q_2 and Q_1^3 sediments) and the lower investigated aquitard (Q_1^{2-3}). The upper aquitard is characterized by higher void ratios, lower unit weights, higher compression indices, and lower coefficients of consolidation compared to the lower aquitard.

Grain-size analyses of seven samples collected between 0.1 and 1.0 m depth at site GW1 indicate that the top soil is dominated by medium to fine silt and clay fractions. (Fig. 8a). For silt, standard values for the Van Genuchten parameters α and n are reported to 0.06 kPa^{-1} and 1.53 along with a residual water content of θ_r (−) of 0.123 (Tuller and Or, 2005). In Fig. 8b to f, the measured SWCC are presented for the samples between 0.3 and 1.0 m. Note that only a subset of the measured data was used for the fits of the Van Genuchten parameters to prevent the large number of measurements (>100) at low matric potential Ψ, from disproportionately dominating the information content of the single measurement at higher Ψ (see Fig. 8). Based on these characterizations, Van Genuchten parameters of α = 0.04 kPa^{-1} and $n = 1.4$ are utilized for the model with a residual water content of θ_r (−) of 0.123.

3.3. Numeric simulation of land subsidence

The numeric simulation of land subsidence due to groundwater depletion at the monitoring site GW1 in the southern VMD provides calculated subsidence dynamics along the modeled 500 m × 81 m cross-section for the period 1990–2025. In the present study, three distinct simulations are employed, either supposing (i) undisturbed subsurface

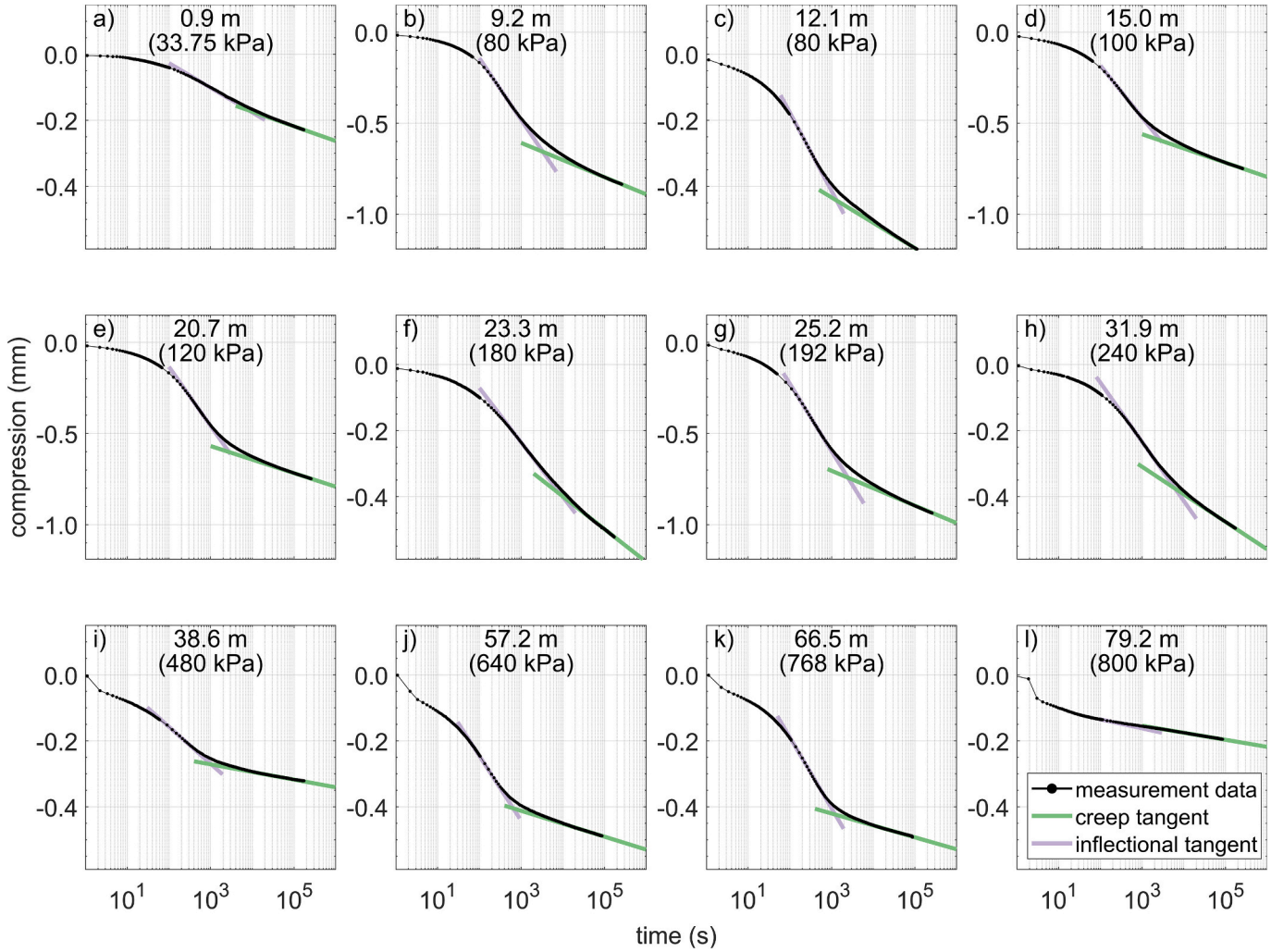

Fig. 6. Time-compression curves from twelve one-dimensional compression tests on undisturbed drill core samples from GW1 between 0.9 m and 79.2 m depth. The respectively evaluated incremental load stages are displayed in brackets below the samples' depth information.

sediment strata, (ii) subsurface disturbances due to a single well-casing failure or (iii) subsurface disturbances due to multiple well-casing failures implemented into the model in 3 m intervals along the casing.

Fig. 9 illustrates calculated subsidence dynamics for the simulation period 1990–2025. The degree of spatiotemporal heterogeneity in computed subsidence rates varies significantly between the three simulations employed for the period 1995–2025, during which groundwater depletion occurs. In the simulation which considers undisturbed subsurface strata, a subsidence rate of 5.1 mm a^{-1} (Fig. 9a) is calculated for the monitoring site GW1, which is situated in approximately 5 m distance to an aquaculture pond. An equal subsidence rate of 5.1 mm a^{-1} is calculated for an urban area, whereas the road experiences lightly elevated subsidence rates of 5.7 mm a^{-1} due to the vehicle load of 10 kPa (Fig. 9a). The calculated subsidence rates show seasonal variations, which are induced by the implemented sinusoidal water load of the aquaculture ponds.

Including a local subsurface disturbance in form of a single well-casing failures into the model yields in notably different spatiotemporal subsidence dynamics, increasing calculated subsidence rates to 6.3 mm a^{-1} and 6.5 mm a^{-1} for the well and road location respectively (Fig. 9b).

Including local subsurface disturbances in form of multiple well-casing failures, implemented into the model in 3 m intervals along the casing, yields in significantly more expressed spatiotemporal subsidence dynamics (Fig. 9c). For the monitoring site GW1, the calculated subsidence rates increase only marginally from 5.1 mm a^{-1} to from 5.6 mm a^{-1} under consideration of multiple well-casing failures in a well in the nearby urban area. Conversely, the road is subject to significantly elevated subsidence rates of 18.1 mm a^{-1}, representing an increase by a factor of 3 compared to the simulation of undisturbed subsurface sediment strata. The impact of the local well-casing failure on calculated subsidence rates peaks at the location of the implemented well, with calculated subsidence rates of 25.0 mm a^{-1} and a corresponding increase by a factor of 5 compared to the simulation of undisturbed subsurface sediment strata, with multiple well-casing failures implemented into the model at 3 m intervals along the casing.

Fig. 10 visualizes the results for the end of the simulation period in 2025, including the spatial distribution of computed subsidence (Fig. 10a), subsurface vertical strains (Fig. 10b), excess pore pressure (Fig. 10c) and hydraulic head (Fig. 10d) for the respective simulations of undisturbed sediment strata (Fig. 10a to d-i) and local subsurface disturbances due to a single well-casing failure (Fig. 10a to d ii) and multiple well-casing failures in 3 m intervals along the casing (Fig. 10a to d iii).

Fig. 10a-i shows a near-uniform horizontal distribution of land subsidence with a maximum subsidence below the road and minimum subsidence below the ponds. Conversely, the implementation of local subsurface disturbances due to well-casing failure induces a local peak maximum of subsidence at the well location, resulting in a horizontally heterogeneous subsidence distribution (Fig. 10a-ii and Fig. 10a-iii).

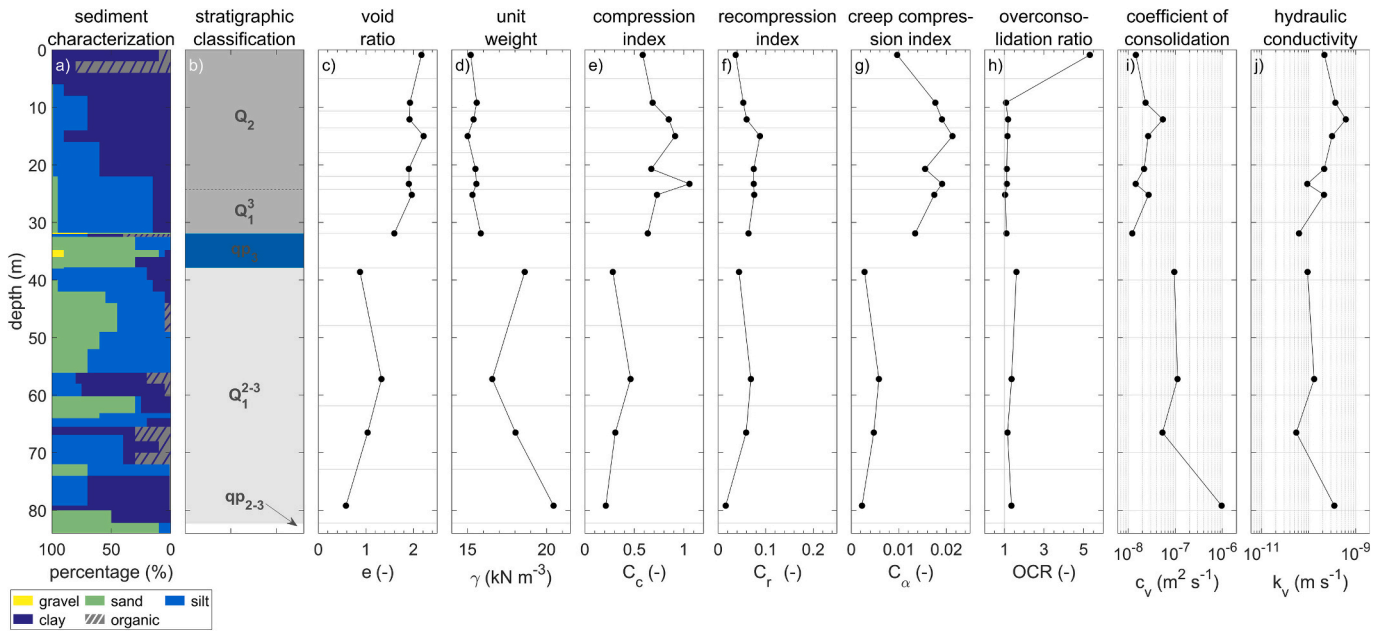

Fig. 7. Profiles showing the geomechanical characterization of the study site GW1 in the southern VMD including a sediment characterization visualized as a stacked percentage of each sediment class (a), a stratigraphic classification (b), and a parameterization void ratio (c), unit weight (d), compression index (e), recompression index (f), creep compression index (g), overconsolidation ratio (h), coefficient of consolidation (i) and vertical hydraulic conductivity (j).

The spatial distribution of subsurface strains is visualized in Fig. 10b and enables a depth-dependent assessment of the sediment compaction, which ultimately induce the subsidence of the groundwater surfaces. Fig. 10 b-ii shows that when a single well-casing failure is implemented in the model, strains are greatest in the vicinity of the failure. Fig. 10 b-iii illustrates that in the presence of multiple damaged well-casing segments, the greatest strains occur in approx. 10–12 m and in 21–23 m depth, where the sediments are highly compressible with high compression indices of C_c = 0.85–1.0 (Fig. 7e). Conversely, in the simulation of undisturbed sediment strata, strains are greatest in the second lowest layer of Q_1^{2-3} aquitard, where the compression index is significantly lower with $C_c = 0.31$. These distinct strain distributions are induced by the specific hydraulic head distributions (Fig. 10d) within the two simulations. In the simulation of undisturbed sediment strata, a predominantly uniform distribution of hydraulic head is computed (Fig. 10d-i), whereas at each implemented damaged casing segment the hydraulic head is locally determined by the reference head of the implemented drain boundary condition (Fig. 10d-ii and Fig. 10d-iii). This reference head corresponds to the water level within the casing and is equivalent to the head of the tapped aquifer qp_{2-3}. Given that the dissipation of excess pore pressure is associated with drainage and associated compaction, the excess pore pressure is indicative for pending compaction and hence subsidence, which has to be anticipated as a delayed response to past groundwater depletion. It is noted that in the employed fully coupled flow-deformation model, the excess pore pressure is defined by the difference between the actual pore water pressure and the pore water pressure in a steady-state flow condition. An individual presentation of these pressure distributions is presented in supplementary information S5. In the simulation of undisturbed sediment strata, in 2025 the excess pore pressure is greatest in approx. 60 m depth (Fig. 10c-i), where hydraulic conductivity is low and the distance to the draining aquifers qp_3 and qp_{2-3} is large (Fig. 7b and j). Fig. 10c-ii and Fig. 10c-iii show that at each implemented damaged casing segment, the excess pore pressure equals to zero, given that water can be drained from the subsurface sediments into the well-casing. The vehicle load on the road as well as the distribution of sealed surfaces (no-flow boundary conditions) and vegetated surfaces (seepage boundary conditions) leads to the complex distribution of excess pore pressure as illustrated in Fig. 10c-ii and Fig. 10c-iii. It is noted that for a direct comparison of the simulated excess pore pressure distributions (Fig. 10 c), it must be considered, that due to the well-casing failure, the steady-state groundwater flow conditions differ between the simulations, given the local assimilation of hydraulic heads in the aquitard layers toward the head in the tapped aquifer qp_{2-3}.

The contribution of suction pressure to the total effective stress is minor, remaining below 2 kPa in the simulation with undisturbed sediment strata (Fig. 11a) but increases locally to approx. 3.5 and 10 kPa beneath sealed surfaces in the simulation that additionally accounts for single or multiple well-casing failures respectively (Fig. 11b and c).

To provide a quantitative assessment of model performance, the simulated subsidence time series are compared with the observed subsidence data at monitoring site GW1 and its vicinity (Fig. 12). The scenario with multiple well-casing failures is shown explicitly in the comparison. As demonstrated in the evaluation of the different simulation scenarios (no well-casing failure, single well-casing failure, and multiple well-casing failures), the simulated subsidence behavior at the non-urban monitoring location GW1 remains nearly identical across all scenarios, whereas pronounced spatial variability emerges mainly in the vicinity of the implemented well casing. Consequently, the comparison illustrates both the subsidence dynamics at GW1 and the potential for strong local heterogeneity represented by the multiple well-casing failure scenario. The root mean square error (RMSE) is calculated to 1.1 mm for monitoring site GW1 using the average of the measured subsidence time series at GW1 and the corresponding simulation results for the same location. Compared with the median vertical measurement misclosure of 0.29 mm across the 35 geodetic monitoring campaigns, the RMSE of 1.1 mm indicates that model deviations exceed the internal survey precision but remain relatively small in absolute magnitude. It should be noted that this evaluation is site-specific to GW1 and does not assess predictive model performance with respect to spatial variability beyond this location. In addition, residual deviations at GW1 may partly reflect processes not explicitly represented in the model, such as auto-compaction. The model should therefore be understood primarily as a process-based exploratory tool rather than a precise predictive framework for total land subsidence arising from all contributing drivers.

It should be noted that the aim of the modelling is not to claim that

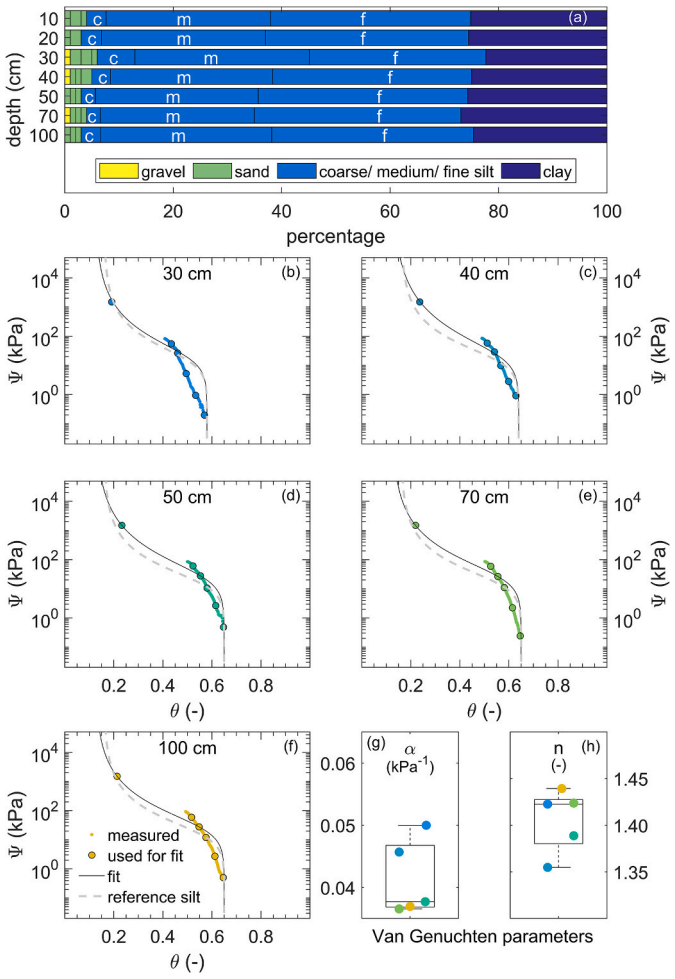

Fig. 8. Grain size distribution (a) and soil water characteristic curves (b-f) for soils in the top first meter at GW1 and resulting Van Genuchten parameters (g-h).

the observed spatial heterogeneity in subsidence rates must necessarily be explained solely by well-casing failures. Rather, the modelling follows an exploratory approach. It demonstrates that the observed subsidence trend and parts of the temporal dynamics at the GW1 site, represented in the model through sinusoidal surface loading variations, can be reproduced in the correct order of magnitude, while acknowledging that additional processes, such as heterogeneity in geomechanical properties and spatially and temporally variable groundwater depletion, also influence the real subsidence dynamics.

This comparison shows that seasonal surface loading due to variations in surface water levels can influence subsidence dynamics in a manner comparable to seasonal variations in groundwater extraction. At the same time, the simulations illustrate that well-casing failures, depending on their extent, may represent a plausible mechanism contributing to the development of pronounced spatial heterogeneity and local extremes in subsidence rates.

The future contribution of delayed subsidence resulting from previous groundwater depletion is assessed in a scenario simulation assuming stable groundwater heads after 2025. As shown in Fig. 13a considering undisturbed sediment strata, the delayed subsidence response leads to an additional increase of 0.14–0.18 m yielding and a total subsidence of 0.30–0.35 m by 2100, with only minor differences between non-urban and urban landscapes. The simulations that account for single and multiple well-casing failures (Fig. 13b and c) yield comparable cumulative subsidence for the non-urban monitoring site GW1. Conversely, the well-casing failure and the associated assimilation of hydraulic heads in the aquitard layers toward the head in the tapped aquifer $qp_{2–3}$ exacerbate urban subsidence, yielding a calculated cumulative subsidence of 0.42–0.44 m by 2100 for single well-casing failure and 1.15–1.35 m when considering multiple well-casing failures.

4. Discussion

4.1. Geomechanical subsurface characterization and implications on subsidence dynamics

The results show a high compressibility of the Holocene and Pleistocene aquitards Q_2 and Q_1^3, indicating their high potential for compaction and land subsidence. The depth-differentiated mean value of $C_c = 0.77$ in these aquitards at GW1 (Fig. 7e) exceeds reported spatial mean compression indices of $C_c = 0.66$ for soft clay Holocene deposits in the VMD (Baldan et al., 2025). The variation of C_c along the presented depth profile (Fig. 7e) underscores that utilizing mean values for C_c within hydrogeological units in geomechanical simulations is a simplification, which may require careful reconsideration for accurate and high-resolution simulations.

The geomechanical characterization reveals predominantly normally consolidated conditions along the depth profile in the Holocene aquitard Q_2 and the upper Pleistocene aquitard Q_1^3. Only in the topmost

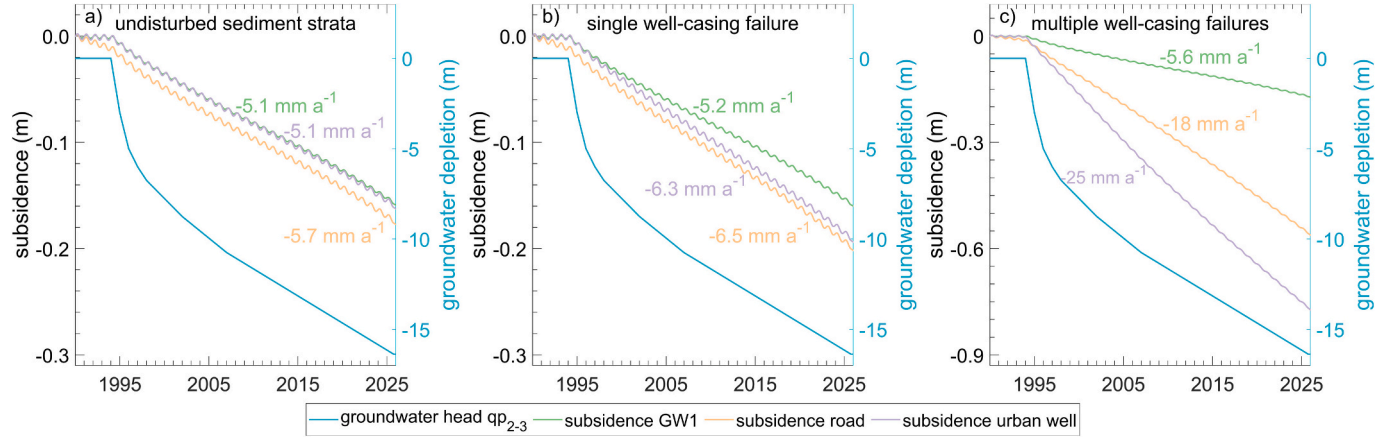

Fig. 9. Simulated land subsidence induced by groundwater depletion and local surface loading along a road (a), and with additional consideration of a single well-casing failure (b), and multiple well-casing failures (c) for the period 1990–2025 at monitoring site GW1 in the southern VMD. Note that in (a) the time-series of subsidence at GW1 and at the urban well are nearly equal, therefore hard to distinguish. Also note the different y-axis scale in (c) and that additionally to groundwater head depletion in $qp_{2–3}$ the model considers groundwater depletion in qp_3 aquifer (see Fig. 1a).

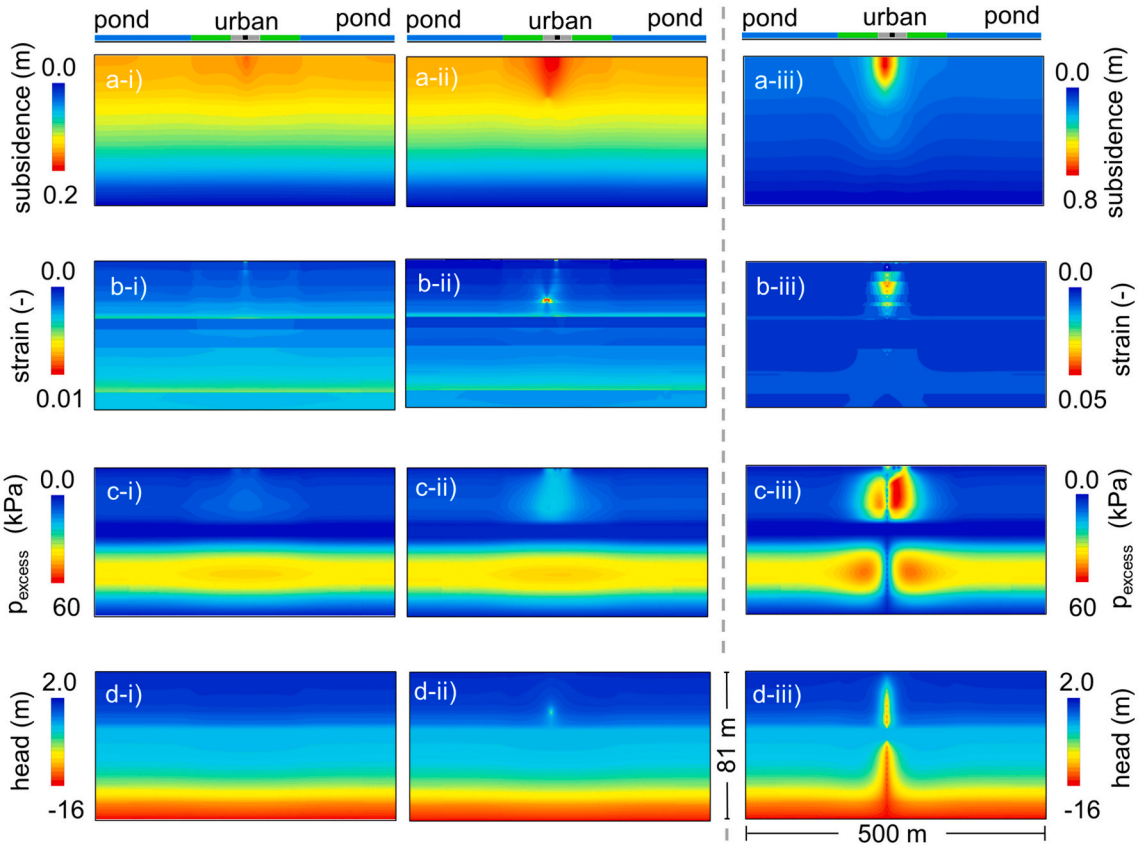

Fig. 10. Simulated state variables at the end of the simulation period (2025), showing vertical displacement (i.e., subsidence) (a), vertical strain (b), excess pore pressure (c), and hydraulic head (d), for scenarios with groundwater depletion and surface loading from a road (i), and with additional consideration of a single well-casing failure (ii) and multiple well-casing failures (c). Note that the y-axis scales in (a-iii) and (b-iii) differ from those in (a-i) to (b-ii). Surface land-use characteristics are schematically shown in the upper part of the figure (see Fig. 2 for details).

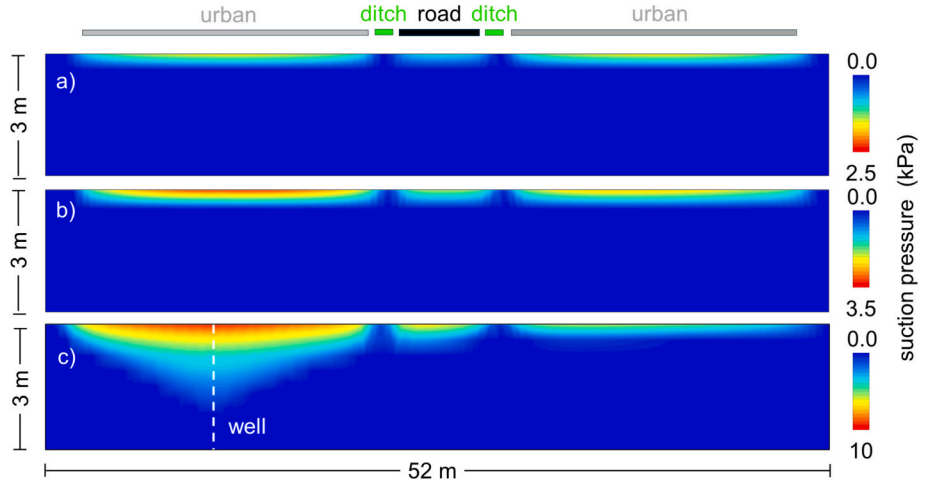

Fig. 11. Calculated suction pressure at the end of the simulation period (2025) for scenarios with groundwater depletion and surface loading from a road (a), and with additional consideration of a single well-casing failure (b) and multiple well-casing failures (c).

meters, the sediments are characterized by overconsolidated conditions. Similar *OCR*-profiles have been reported by Mi et al. (2023) for Holocene deposits in the southern VMD, characterized by lightly to moderately overconsolidated conditions in the top 4–5 m thick weathered crust and a convergence of *OCR* toward unity with increasing depth. The *OCR*-profile at GW1 implies that except for the top meters, deformation processes are characterized by the compression index C_C and therefore must be anticipated to be only marginally reversible. The potential of sediments to revert compression when the effective stresses are reduced is characterized by the recompression index (Allen and Mayuga, 1970). The results show that the compression index exceeds the recompression index by a factor of 9.0 to 15.8. This indicates that once the sediments undergo inelastic deformations, the land rebound potential is limited to approx. 6–11% (inverse of 9.0 and 15.8) of the inelastic deformation.

The derived vertical hydraulic conductivity for GW1 (Fig. 7j) varies between 6.3 $\cdot 10^{-11}$ and 6.2 $\cdot 10^{-10}$ m s^{-1} along the vertical profile,

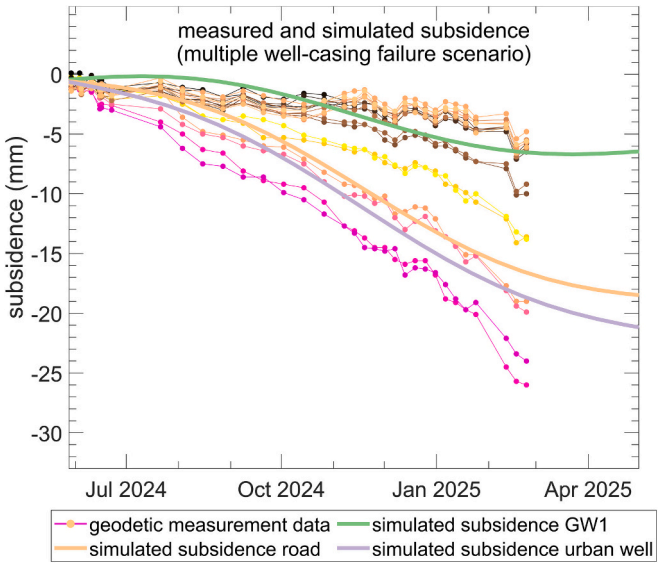

Fig. 12. Comparison of measured and simulated subsidence dynamics for the multiple well-casing failure scenario.

thereby agreeing with literature values for unweathered marine clay (Domenico and Schwartz, 1998) like the Q_2 and Q_1^3 deposits in the southern VMD (Wagner et al., 2012). Due to the low hydraulic conductivity in combination with the aquitard thicknesses of 31.9 m and 44.3 m, dissipation of excess pore pressure and the associated aquitard drainage are slow processes, and a delayed subsidence response to past groundwater depletion must be anticipated. This is also manifested in the coefficient of consolidation, c_v, a parameter which describes the rate of sediment compaction. The calculated values of c_v between $1.2 \cdot 10^{-8}$ and $5.4 \cdot 10^{-8}$ $m^2\ s^{-1}$ in Q_2 and Q_1^3 (Fig. 7i) corroborate previous analyses of c_v in the study area Ca Mau, characterized by a range of $c_v = 2.9 \cdot 10^{-8}$ to $1.1 \cdot 10^{-9}$ $m^2\ s^{-1}$ in the Holocene aquitard Q_2 (Nguyen Thi et al., 2020). The distinct variation in parameter characteristics between the upper and lower aquitard is consistent with classifications of very soft to soft clay in the near-surface aquitard and medium to stiff clay in the lower aquitard (Mi et al., 2023), reflecting differences in depositional history and consolidation characteristics.

The high compression indices together with the predominantly normally consolidated conditions characterize the high potential of the Holocene sediments for land subsidence due to groundwater depletion in the southern VMD. However, with the relatively weak depletion rate in the adjacent aquifer qp_3 (Duy et al., 2021; Fig. 1a) the increase in effective stress within the Holocene deposits over recent decades has remained moderate, leaving the Holocene's high potential for land subsidence largely inactivated. Within the scope of this local-scale study, these findings underline that particularly the exploitation of shallow aquifers (< 40 m depth) and the resulting exposure of the highly compressible sediments to increasing effective stresses must be prevented to avert exacerbating subsidence dynamics. Therefore, this local-scale analysis highlights that informed sustainable water resource management is essential with a particular emphasis on the regulation of shallow aquifers, which are of particular interest for aquaculture due to their predominantly brackish water quality. Given the low hydraulic conductivity and substantial thickness of the aquitards, a considerable portion of the subsidence will occur with delay, emphasizing the necessity for proactive water management practices.

Beyond the presented local geomechanical parameterization in high vertical resolution, a spatially extensive depth-differentiated mapping of geomechanical properties is crucial for robust predictions of delta-wide subsidence in the southern VMD. Despite seemingly similar lithologic compositions, Holocene sediments can exhibit spatially highly heterogenous geomechanical characteristics, governing their consolidation behavior and additionally contributing to the spatial complexity of observed subsidence patterns (Buffardi et al., 2025). This highlights the need for improved geomechanical parameterization at higher vertical and horizontal resolution in the VMD, to support both high-resolution modelling and the derivation of representative parameters for more generalized approaches.

4.2. Spatiotemporal dynamics of observed land subsidence rates

The two evaluated subsidence datasets of geodetic leveling data (Fig. 3) and InSAR-derived subsidence rates (Fig. 4) show consistent patterns of spatial heterogeneity of comparable order of magnitude. As these datasets cover non-overlapping time periods and the geodetic leveling data cover only a subset of the spatial extent of the local InSAR data, the agreement between them remains qualitative in nature, with no possibility of direct comparison. Nevertheless, both datasets exhibit similar characteristics with regard to the magnitude and extent of subsidence heterogeneity, which supports their interpretation as plausibly consistent. While the geodetic leveling data show moderate subsidence rates <10 mm a^{-1} at the non-urban monitoring site GW1, approximately 90% of the individual InSAR scatterers in the vicinity of GW1 show subsidence rates greater than those derived from leveling at GW1. This local analysis may indicate that the InSAR-based assessments of land subsidence are not necessarily representative for non-urban landscapes in the southern VMD. In addition, even within urban areas, high variability in InSAR-based subsidence rates have been reported earlier (e.g.

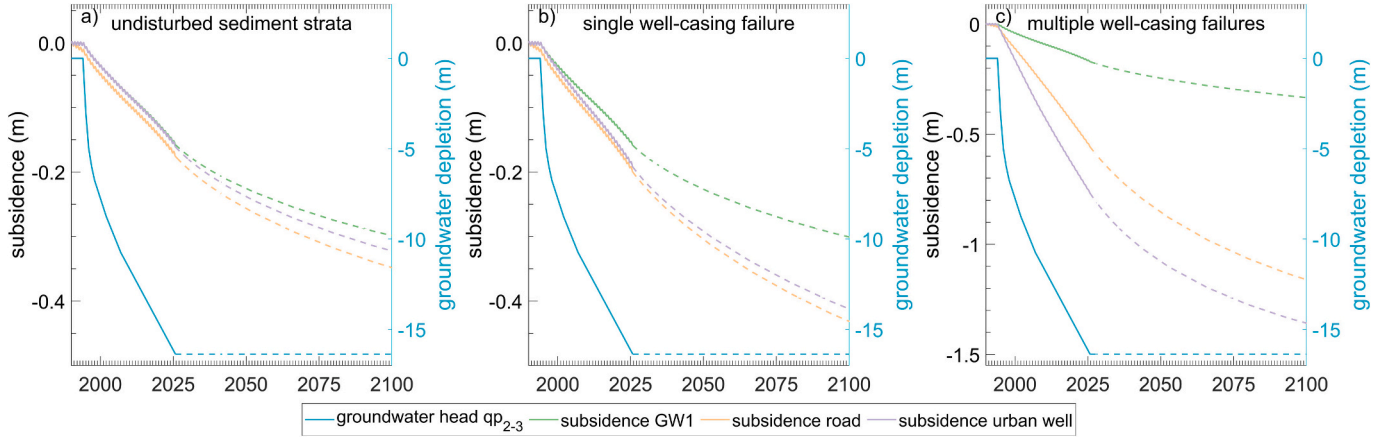

Fig. 13. Simulated delayed future subsidence assuming no further groundwater depletion for the period 2025–2100 at monitoring site GW1 in the southern VMD (a) and with additional consideration of a single well-casing failure (b) and multiple well-casing failures (c). Note the different y-axis scaling in (c).

Minderhoud et al., 2018), particularly in urban areas, where this variance has been attributed to buildings' specific type and depth of foundations and previous land use (De Wit et al., 2021). While the present geodetic leveling results also reveal a similarly high variability in subsidence, the monitored points are not directly located on surfaces exposed to loading, such as roads or buildings, but rather in intermediate and adjacent zones without direct surface loading. The ground-based geodetic data, albeit limited to only a few points, does not show a correlation between elevated subsidence rates and distances to loading infrastructure e.g. the road or buildings. This suggests that, in addition to groundwater depletion and surface loading, other contributing processes or environmental conditions with high spatial variability could be at play, inducing the hazardous subsidence rates derived from delta-wide InSAR analyses. Future research would benefit from more extensive geodetical monitoring campaigns, allowing for a statistically sound evaluation of potential relationships between subsidence dynamics and distances to certain infrastructures or land use types.

The subsidence rates derived from the geodetic monitoring campaign are subject to uncertainties, as the depth of the bridge's pile foundation, and thus the depth datum representing the zero level of the subsidence measurements, is uncertain. Consequently, any sediment compaction occurring below the bridge's foundation level, and the associated land subsidence, are not captured in the geodetic observation data. While using the nearby bridge as a stable reference point follows the general approach of Dörr et al. (2024), who employed larger (~200 m) bridges together with solid rock outcrops as reference networks for InSAR analyses in the southern VMD, the bridge in this study is shorter (~50 m). Nonetheless, the agreement between the subsidence rates derived from the geodetic monitoring campaign (Fig. 3) and the InSAR satellite data (Fig. 4) suggests that the bridge at the study site serves as a reasonably reliable reference point for subsidence observations. For future studies, it is recommended to obtain and incorporate actual data on bridge foundation depths to clarify the corresponding depth datum, while GNSS (Global Navigation Satellite System) measurements could additionally be employed to provide an absolute vertical reference.

Overall, for the observation of land subsidence dynamics, space-borne methods have become indispensable, providing valuable datasets on spatiotemporal subsidence dynamics in the VMD since more than a decade (Dörr et al., 2024; Erban et al., 2014). However, such methods are limited to the observation of persistent or temporal scatter points like rooftops of buildings or road surfaces and are incapable of monitoring subsidence dynamics of natural environments like vegetated surfaces. The local-scale study supports the interpretation, that the inherent overrepresentation of anthropogenically shaped land in delta-wide InSAR-based subsidence analyses possibly undermines their representativeness for regional dynamics in non-urban dominated landscapes. This potential limitation of InSAR based observations underscores the relevance of ground-based monitoring as well as physic-informed modelling, as proposed in this local-scale investigation.

The spatial heterogeneity of subsurface properties and groundwater extraction patterns limits a direct extrapolation of the process quantification at GW1 to the entire delta and limits overgeneralizing the derived management implications. However, the process dynamics identified at GW1 can be considered broadly representative of the southern VMD for several reasons: (i) The stratigraphy at GW1 falls within the range of reported layer thicknesses and lithological configurations documented for the southern VMD (e.g., Wagner et al., 2012; Duy et al., 2021; Mi et al., 2023) and compression indices are broadly comparable to those reported by Baldan et al. (2025). (ii) The observed groundwater head declines at GW1 are comparable to those reported from other parts of the southern delta (Duy et al., 2021; exemplary also Fig. 1a). (iii) The aquaculture-dominated land use, with minor adjacent urban infrastructure along a road corridor, reflects typical land-use and land-cover characteristics of large parts of the southern VMD. (iv) InSAR-derived subsidence rates in the vicinity of GW1 are comparable in magnitude and spatial variability to delta-wide observations (Dörr et al., 2024). (v) The quantified subsidence dynamics due to groundwater depletion are in overall agreement with results from delta-wide numerical modelling studies (e.g., Minderhoud et al., 2017). Together, these aspects support the relevance of the identified hydro-geomechanical process dynamics beyond the immediate study site, while acknowledging that local variability across the delta may lead to differences in the relative contribution and timing of individual drivers.

4.3. Simulated land subsidence due to groundwater depletion

This study presents a fully-coupled flow-deformation model that applies geomechanical parameterization at high vertical resolution to simulate local land subsidence dynamics in the southern VMD. Utilizing this advanced simulation approach at local scale for a detailed 2-D cross-sectional model complements delta-wide benchmark simulations on land subsidence due to groundwater depletion in the VMD by Minderhoud et al. (2017, 2020). Overall, the presented local-scale modelling results support the validity of the delta-scale estimates of land subsidence due to groundwater depletion introduced by Minderhoud et al. (2017), thereby countering previously raised concerns regarding model-structural uncertainties and the resulting skepticism toward their projections. This interpretation is consistent with recent investigations by Lexmon et al. (2025), which demonstrate that vertical aquitard discretization exerts a negligible influence on subsidence estimates at the delta scale in the VMD.

In the model simulation for fully undisturbed sediment strata, a land subsidence rate of 5.1 mm a^{-1} is calculated for the non-urban monitoring site GW1. This simulated rate represents the lower bound of subsidence values observed in delta-wide (Dörr et al., 2024) and local (Fig. 4) InSAR analyses, but is generally consistent with computed subsidence rates by Minderhoud et al. (2017), who calculated an average delta-wide subsidence due to groundwater depletion of 18 cm over 25 years, equivalent to a rate of 7.2 mm a^{-1}. However, a direct comparison is not feasible because the model domains differ in their vertical extent and Minderhoud et al. (2017, 2020) report total subsidence without depth differentiation of the governing compaction processes. By presenting the first depth-differentiated simulation results of subsidence caused by groundwater depletion in the Mekong Delta, this local-scale study illustrates how depth-differentiated simulations can support more robust assessments of how the exploitation of specific aquifers can affect subsidence vulnerability (see Section 4.6).

The difference between the simulated (5.1 mm a^{-1}) and observed (8 mm a^{-1}) subsidence rates at GW1 might be attributed to process dynamics not captured with the proposed model, e.g. autocompaction. However, without reliable information on the depth of the bridge's pile foundation, and thus the reference depth of the subsidence measurements, this attribution remains uncertain.

In the simulation results, the influence of locally unsaturated conditions on shallow compaction is minor and mainly restricted to sediments below sealed surfaces, as the aquaculture ponds maintain fully saturated conditions in the soils below. The limited impact arises from the shallow depth range affected by the lowering of the phreatic water level within the Holocene aquitard, resulting in only minor and spatially restricted increases in effective stress (Fig. 11a). It is noted that the adopted van Genuchten parameters do not optimally reproduce the measured $\Psi - \theta$ relationship in the near-saturation range, but were selected to represent literature values typical for the local silt-dominated sediments. However, as the sediments remain almost fully saturated in all three employed simulations (minimum saturation $> 95\%$), the influence of the resulting slight overestimation of suction pressure on the simulated subsidence dynamics is minor. The largely saturated conditions are controlled by the low vertical hydraulic conductivity and the anisotropy ratio (k_h/k_v), which together restrict vertical percolation and promote shallow lateral flow from fully saturated sediments beneath aquaculture ponds toward the unsaturated zones below sealed surfaces. In urban settings, however, such as in the provincial capital Ca Mau City,

the extent of sealed surfaces is considerably larger, lateral flow becomes less effective and declines in the phreatic water level within the Holocene aquitard may be anticipated. This would in turn induce spatially more pronounced unsaturated conditions, thereby exerting a greater influence on sediment compaction and resulting land subsidence. The quantified impact of unsaturated conditions substantiates the discussions of De Wit et al. (2021), who postulate that urbanization may accelerate subsidence due to lowered phreatic groundwater levels.

The land subsidence time series computed in the present study exhibit seasonal variations (Fig. 9), consistent with seasonal patterns observed in local InSAR data (Fig. 4c). Indications of temporal variability are also visible in the geodetic leveling data at GW1 (Fig. 3b), although the available observation period is too short to robustly resolve a seasonal signal. In the simulation results, the seasonal variations are attributable to the sinusoidal representation of water load fluctuations in aquaculture ponds acting on the ground surface. This indicates that a correlation between the seasonal characteristics of subsidence and groundwater dynamics does not necessarily imply a causal relationship, as both processes are governed by the same seasonal surface load variations. Imprints of this interrelation can also be inferred on sub-seasonal scales from observed subsidence rates and groundwater heads e.g. during January and February 2025 (Fig. 3a), for instance during periods of temporarily rising or rapidly declining groundwater heads. In addition to loading-induced seasonality captured in the model, seasonal groundwater abstraction for agriculture or domestic water supply may also contribute to seasonal variations in groundwater heads and associated subsidence dynamics. In the present modelling framework, groundwater extraction is represented through annual average depletion rates, which simplifies potential seasonal variability in pumping-induced head dynamics. Recent analyses for the investigated pilot site GW1 (Dörr et al., 2026) indicate that the majority of the observed seasonal variability in groundwater heads is induced by loading effects, whereas loading-corrected, and therefore abstraction-induced, seasonal fluctuations appear to have a comparatively minor influence on the annual variation of groundwater head dynamics at this local setting.

The implementation of a vehicle load of 10 kPa does not result in significant additional subsidence of the road (see Fig. 9a). Building loads, which are not included in the simulation, likely exert a similar magnitude of loading as the implemented 10 kPa vehicle loads (Xu et al., 2025). This suggests that the evaluated combination of laterally uniform groundwater depletion and local urban surface loading alone is insufficient to either explain the spatially heterogeneous patterns of observed subsidence (Fig. 3 and Fig. 4) or the regionally reported hazardous subsidence rates of up to 30–50 mm a^{-1} (Dörr et al., 2024; Erban et al., 2014) under the assumption of laterally uniform parametrization and boundary conditions utilized in the present model. In addition to the numerically assessed impact of well-casing failure, other localized drivers and subsurface heterogeneities not explicitly represented in the modelling framework are likely to contribute to the observed subsidence patterns, such as shallow drainage, historical land-use changes, spatially variable groundwater head depletion, or small-scale heterogeneities in geomechanical properties and layer thickness.

The simulation results reveal a pronounced delayed subsidence response to past groundwater depletion, amounting to an additional 0.14–0.18 m and a total subsidence of 0.30–0.35 m by 2100 (Fig. 13a). This projection is consistent with the M2-scenario of Minderhoud et al. (2017), who estimated a comparable future subsidence of approx. 0.20 m and a total subsidence of approx. 0.40 m by 2100 under the assumption that groundwater depletion ceased in 2018. It should be noted that the assumption of stable groundwater heads after 2025 represents an optimistic and most likely unrealistic groundwater management scenario given current extraction trends. In this study, the assumption primarily serves to isolate and quantify the delayed subsidence response to groundwater depletion that has already occurred in the past. The magnitude and temporal evolution of this delayed response may differ under alternative groundwater management scenarios, such as continued business-as-usual depletion or a recovery of groundwater heads, for example through managed aquifer recharge.

4.4. Well-casing failure as a potential factor for spatiotemporal heterogeneity in subsidence dynamics

To explore potential factors contributing to the pronounced spatiotemporal heterogeneity in observed subsidence rates, the possibility is examined that failures in borehole casings can provide local subsurface drainage pathways and hydraulic interconnectivities, thereby facilitating accelerated aquitard drainage and compaction. In general, well-casing failures and ruptures in borehole casings are well known consequences of land subsidence induced by groundwater depletion (Gambolati and Teatini, 2021; Holzer and Johnson, 1985). However, to the best of the authors' knowledge, it has not yet been proposed that once such casing damage occurred, it can also accelerate subsequent subsidence by providing local subsurface drainage pathways and a local equilibration of hydraulic heads between the aquitard and the tapped aquifer.

By implementing damaged well casing segments into the model, spatially heterogeneous subsidence rates were simulated, with peak subsidence occurring at the locations of the failed well-casings. The simulated local subsidence peaks in the vicinity of the well are caused by two processes, namely (i) acceleration of compaction processes by provision of drainage facilities and (ii) locally increased groundwater head depletion. Firstly, within this proposed conceptual framework, compaction processes are locally accelerated because well-casing failures provide additional drainage pathways for excess pore water pressure from aquitard sediments into the well casing. In undisturbed settings, aquitard drainage is predominantly directed vertically toward the adjacent aquifer, which can result in a pronounced delay in the presence of thick confining units. In contrast, where well-casing failures occur, drainage is accelerated due to additional, localized, and shorter horizontal flow paths toward the casing. Secondly, this process not only alters the time dependency of compaction but may also affect its overall magnitude. In the present setting, compaction of the shallow Holocene strata is primarily controlled by hydraulic heads in the moderately depleting shallow aquifer. However, drainage toward a well-casing failure is governed by the hydraulic head within the casing, which corresponds to the hydraulic head of the deeper aquifer in which the well is screened. This process is also evident in the computed hydraulic heads in the simulation results (Fig. 10 d).

These processes are schematically visualized in Fig. 14, illustrating how well-casing failure creates drainage pathways for excess pore water pressure dissipation in aquitards and locally exposes aquitard sediments to the lower hydraulic head of the tapped aquifer (denoted as reference head h_2 in Fig. 14) at the casing–aquifer interfaces.

Overall, the simulation results show that damaged well casing segments can potentially provide subsurface drainage pathways and locally accelerate sediment compaction and resulting land subsidence. The simulation results show that the magnitude of this effect strongly depends on the number of well-casing failures considered. To constrain the possible range of impacts, two end-member scenarios were therefore simulated: a single well-casing failure at depths of highest subsurface strain, and multiple failures implemented at 3 m intervals along the casing, conceptually representing failures at each casing joint.

This relationship was further investigated through a sensitivity analysis, in which the magnitude of simulated subsidence was evaluated by varying the number of implemented broken well-casing segments, reducing it from 25 (every 3 m) to 13 (every 6 m), to 6 (every 12 m), and finally to only 2 segments and 1 segment (placed at depths where strains are greatest and casing rupture is therefore most likely). Fig. 15a illustrates the resulting variation in calculated subsidence at the well location at the end of 2025 for different numbers of broken well-casing segments implemented in the model. The results indicate that the magnitude of locally elevated subsidence increases with the number of

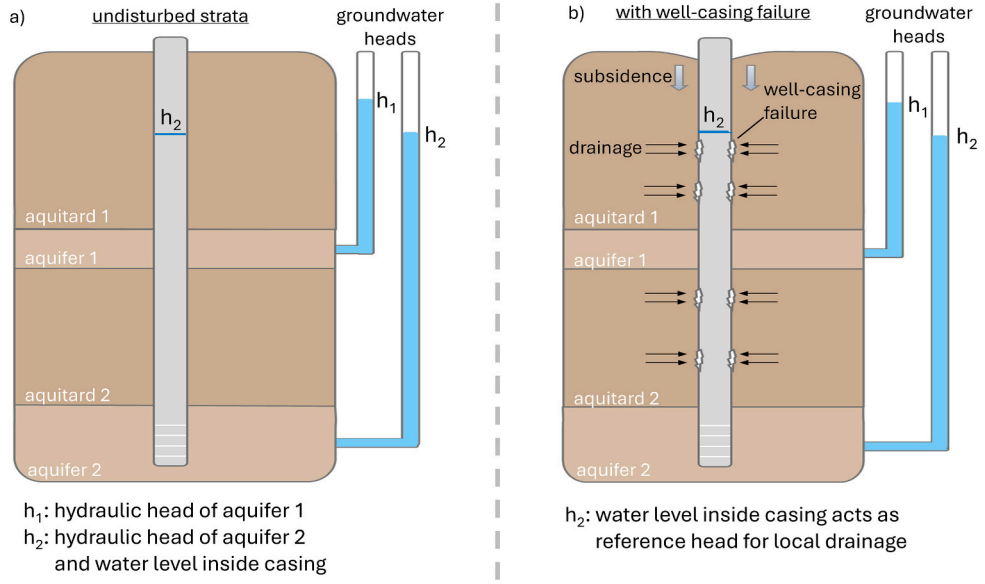

Fig. 14. Schematic illustration of how well-casing failure (b) can accelerate land subsidence compared to an undisturbed subsurface setting (a).

casing failures, highlighting the overall importance of casing integrity and installation quality. An additional sensitivity analysis with respect to the length of the implemented casing-failure segments showed only minor differences in the resulting subsidence when failures were considered every 3 m (Fig. 15b), indicating that the model results are largely insensitive to the exact segment length for the failure spacing considered here.

The scenario assuming casing failures at 3 m intervals represents damage occurring at each casing joint, which can constitute structural weak points of well casings when improperly installed. Such a high number of failures reflects a maximum-impact scenario and would likely require severely compromised casing integrity, for example in cases where the commonly used PVC joints between the 3 m pipe segments in unprofessionally constructed household wells are only loosely fitted or inadequately glued. Previous studies have also addressed the possibility that such household tube wells in the VMD may lose casing integrity over time and thereby potentially affect groundwater quality (Danh and Khai, 2015). Therefore, this scenario is considered to represent a high, yet not necessarily implausible, level of casing damage in individual wells, given the questionable technical quality of unlicensed groundwater extraction wells in the VMD, where improper installation or subsequent weakening of casing joints may result in failures at multiple casing connections within a single well.

Overall, the magnitude and spatial relevance of well-casing failures for subsidence dynamics under field conditions remain difficult to quantify and are subject to considerable uncertainty given the limited availability of observational field evidence. Future field investigations could help test this numerically derived hypothesis, for example through camera inspections of abandoned wells combined with comparisons to InSAR-derived subsidence patterns.

In the VMD, an estimated number of up to half a million to one million unlicensed groundwater extraction wells (Danh and Khai, 2015) provides a spatially extensive and unsupervised subsurface infrastructure of questionable technical quality, with a potential to scale well-

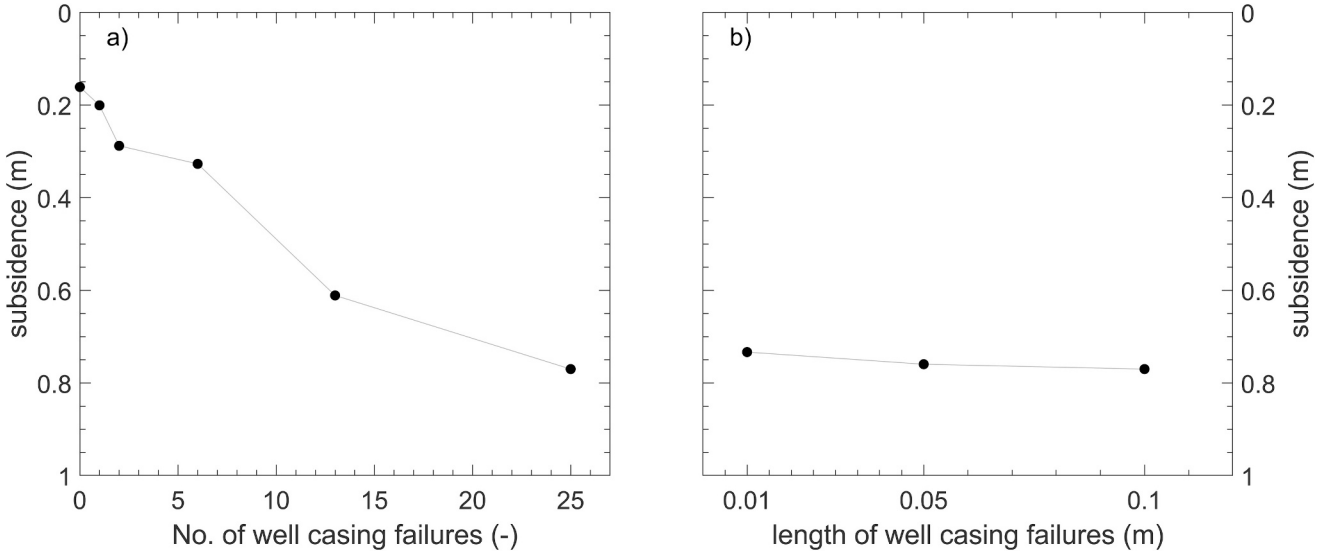

Fig. 15. Calculated subsidence at the well location at the end of 2025 for varying numbers of broken well-casing segments implemented in the model with a constant failure length of 10 cm (a), and for varying well-casing failure lengths with a constant failure spacing of 3 m (b).

casing failure from a local to a regional effect. The proposed process pathway of well-casing failure as land subsidence accelerator may have remained unrecognized because such effects are difficult to infer from surface observations alone, as groundwater wells commonly coincide with local subsidence maxima associated with groundwater depression cones.

The numerically assessed hypothesis of broken well-casings and the resulting interconnectivity of aquifers/aquitards could also offer explanations for other unresolved questions, such as inconsistent hydrogeochemical or isotopic signatures across different aquifers (Osenbrück et al., 2025), and discrepancies between stagnant salinity trends observed in professionally drilled monitoring wells of the NGMN and reported increases in groundwater salinity from farmers' private wells (Hoan et al., 2025). To further evaluate this hypothesis, camera inspections of abandoned wells are recommended. Moreover, mapping the spatial distribution of such wells together with InSAR-derived subsidence scatterers could provide an effective means of validation. Overall, future investigations of well-casing failure effects on land subsidence would benefit from three-dimensional simulations to adequately resolve casing-failure geometries and the resulting localized flow and stress redistribution processes.

While broken well-casing segments would represent unintended subsurface drainage pathways, such drainage effects are recently induced deliberately in the context of road construction in the VMD through the installation of prefabricated vertical drains (PVDs) below newly constructed road embankments (Mi et al., 2023). These are installed to accelerate soil and sediment consolidation immediately after construction and thereby reduce the proportion of compaction and subsidence occurring during operation.

The subsidence observations from the monitoring site GW1 (PW1 and PW2 in Fig. 3 a-b) appear to indicate the presence of potential casing drainage pathways, revealing locally elevated subsidence rates at the multi-extensometer borehole, which is equipped with a sliding-joint casing. Due to the requirement for the sliding-joint casing segments to exhibit flexibility in movement, they are not sealed off against water, therefore representing a small-scale drainage opportunity for the surrounding aquitard sediments. This local drainage to the sliding-joint casing segments is most likely distinctly less pronounced than a potential casing rupture as implemented into the model for an exemplary unlicensed urban production well. This finding supports the hypothesis that well-casing failure accelerates subsidence and, at the same time, raises concerns about the measurement concept of sliding-joint extensometer boreholes, as it suggests that the monitoring facility itself may alter the very compaction dynamics it is designed to observe. Although an additional load from the monitoring installation cannot be fully excluded, the pronounced settlement during the dry season points toward drainage-driven subsurface processes as a likely contributing mechanism.

Overall, the present study corroborates the conclusion of Yuill et al. (2009) that changes in surface and subsurface drainage pathways must be investigated to understand land subsidence and its spatial heterogeneity. With depths of commonly below 3–5 m (Le et al., 2023), the various channels represent possible drainage pathways for the upper few meters of the Holocene deposits in the southern VMD. Therefore, the characteristic street bumps at bridge onsets in the southern VMD (Dörr et al., 2024) may not only be attributable to differential subsidence between the stable bridges' piled foundations and regional subsidence, but also to surface drainage opportunities, accelerating near-surface dissipation of excess pore pressure and associated elevated compaction and subsidence close to the channel bank.

4.5. Capabilities and limitations of the applied modelling framework

The local-scale modelling approach applied here builds upon previous regional modelling studies on groundwater-depletion–induced land subsidence in the VMD (Minderhoud et al., 2017, 2020) by incorporating surface loading from structural loads of the built environment and changing surface water levels, as well as potential anthropogenic subsurface drainage pathways. This enables a process-based exploration of multiple drivers of local subsidence dynamics and their spatiotemporal variability. It should be noted that the implementation of a fully coupled flow–deformation framework per se did not yield fundamentally new insights, as coupling effects have been shown to be minor in comparable problem settings (Gambolati et al., 2000). However, this modelling framework enabled the implementation of surface loading and potential subsurface drainage toward well-casing failures, which, together with the high-resolution, site-specific parameterization, allows for a more detailed investigation of local subsidence processes and their potential drivers.

The employed modelling framework is primarily intended for a process-based exploration of compaction and subsidence mechanisms, whereas precise predictions are constrained particularly due to limited lateral sampling of geomechanical properties. Despite the relatively high vertical data density employed for the geomechanical parameterization, derived from consolidation tests on multiple samples from a single borehole (GW1), the assumption of laterally uniform geomechanical properties within the 500 m lateral model domain represents a simplification, given the inherently heterogeneous geomechanical properties of deltaic sediments (Buffardi et al., 2025). Such unresolved lateral variability in sediment properties, together with possible local variations in groundwater depletion, may affect both the magnitude and spatial distribution of subsidence dynamics beyond the numerically implemented drivers. These assumptions of lateral uniformity limit the generality of the presented results even at the considered local scale.

Overall, the *SoftSoilCreep* model is well suited to simulate the key processes relevant in this study, namely the time-dependent deformation of sediments under groundwater depletion and surface loading (Lee et al., 2018; Feng et al., 2019). However, this constitutive model does not explicitly account for deformation mechanisms associated with cyclic loading. Consequently, deformations due to seasonal loading and unloading of surface water bodies may not be fully captured, representing a limitation of the present simulations. This shortcoming could be addressed in future work by employing constitutive models that incorporate a dedicated description of cyclic deformation behavior.

A general limitation of this study arises from the depth range covered by the available datasets, which only extend to the upper ~80 m of the aquifer system. Consequently, potential contributions to overall subsidence from deeper aquifers and aquitards are not explicitly represented in the model. It should be noted, however, that this depth range corresponds to the portion of the subsurface reflected in the evaluated subsidence observations. In particular, the presented local leveling data is referenced to a bridge foundation that likely extends to comparable depths. Similarly, the InSAR dataset (Dörr et al., 2024) incorporated bridges with deep piled foundations, in addition to rock outcrops, into the reference network. As a result, these observations primarily reflect deformation within the upper ~70–80 m of the subsurface, where most of the measured subsidence was also inferred to originate (Dörr et al., 2024). The focus of the model domain on the upper 80 m and the associated choice of the lower hydraulic head boundary condition limit not only the simulation of compaction in deeper layers but also the assessment of how deep groundwater extraction may influence compaction in shallower strata. This is particularly relevant given the likely limited groundwater recharge (Dörr et al., 2026), as pressure declines induced by deep pumping may progressively affect overlying layers, increasing effective stresses and contributing to land subsidence. To better assess the potential impact of deeper strata on subsidence dynamics, future studies should therefore extend the presented modelling framework to include deeper strata below the upper Pleistocene and evaluate the contribution of deeper groundwater exploitation and aquitard compaction to overall land subsidence.

4.6. Implications for informed mitigation strategies

In subsidence threatened deltas, adaptation and mitigation strategies strongly rely on (i) accurate and representative quantifications of land subsidence across the delta and (ii) a sound process understanding of the driving forces behind land subsidence. Both aspects are essential for reliable predictions of expected future subsidence under various scenario considerations. The present study introduces a high-precision fully-coupled flow-deformation model, exemplary applied on local-scale, as a suitable tool for integrated assessments of land subsidence in the VMD. This study promotes future applications on delta-wide scale that allow the consideration of multiple drivers to support more comprehensive simulation of land subsidence dynamics in the VMD.

The findings of the present local-scale analysis suggest that, to prevent the highly compressible Holocene sediments from being exposed to increasing effective stresses and consequent land subsidence, particularly a depletion of the shallow aquifers *qh* and qp_3 must be avoided. In settings where shallow groundwater is used e.g. for brackish aquaculture, the combined effects of aquifer exploitation and the disconnection of Holocene sediments from surface water through urban sealed surfaces make these areas highly susceptible to intensified land subsidence.

Inter-aquifer connectivity, either caused by natural conditions like faults or hydrogeological windows or by anthropogenic interventions like failures of well-casings or well-bores, can accelerate the assimilation of hydraulic heads in shallow, more compressible strata, toward those of the highly exploited aquifers. Nonetheless, in light of insufficient groundwater recharge (Dörr et al., 2026), even in the absence of inter-aquifer connectivity, the exploitation of deep aquifers and associated head depletions will gradually propagate upward to shallow sediment layers, ultimately exposing them to increasing effective stresses and promoting land subsidence. The findings imply a considerable portion of delayed subsidence to past groundwater depletion at the investigated site in the VMD consistent with previous studies (Minderhoud et al., 2020), emphasizing the overall need for proactive water management strategies demonstrated here through a high-resolution local-scale analysis.

While the presented results highlight potential implications for groundwater management, they are derived from a local-scale analysis and cannot be directly extrapolated to delta-wide conditions. Accordingly, the proposed management implications should be viewed as exploratory rather than prescriptive and require validation at broader spatial scales.

5. Conclusion

The present study substantiates that a detailed depth-differentiated subsurface parameterization is indispensable for accurate simulations of deltaic land subsidence and a reliable subsequent identification of the governing driving processes. Utilizing such sound parameterization in the presented fully coupled flow–deformation model framework provides a comprehensive approach for subsidence simulations, as it enables the integration of various potential drivers and process pathway.

Whilst urban dwellings provide a suitable infrastructure for satellite-based subsidence observations, their influence on compaction processes may concomitantly distort the representativeness of those observations for delta-wide evaluations. This study suggests that beyond the commonly considered effects of urban infrastructure loading and local anomalies in groundwater demand and depletion, sediment compaction below urban areas may also be influenced by anthropogenic subsurface disturbances like damaged well casings. The employed hypothesis-driven exploratory simulations indicate that such local disturbances could accelerate and intensify compaction by creating additional drainage pathways and increasing effective stresses in aquitards through a local assimilation of hydraulic heads toward those of the tapped aquifers. The impact of such effects depends locally on the number and extent of well-casing failures as well as on subsurface characteristics, particularly the aquitard thickness and hydraulic conductivity and at larger scales on the number of affected wells. However, the magnitude of these effects remains uncertain due to limited observational field evidence. Therefore, validation of this numerically assessed hypothesis is recommended, for example, through camera inspections of abandoned wells and their mapping together with InSAR-derived subsidence scatterers.

To mitigate the exposure of the highly compressible Holocene sediments to increasing effective stresses and the associated land subsidence, depletion of the shallow aquifers must be prevented in the Mekong Delta and other deltaic aquifer systems worldwide. In settings where economic activities rely on brackish water from these shallow aquifers, a particular vulnerability to advancing land subsidence must be anticipated. The derived portion of delayed subsidence to past groundwater depletion at the investigated site underscores that proactive water management strategies are crucial for the viability of the southern Mekong Delta.

Abbreviations

GNSS	Global Navigation Satellite System
InSAR	Interferometric Synthetic Aperture Radar
LULC	Land Use and Land Cover
NGMN	Vietnamese National Groundwater Monitoring Network
OCR	Overconsolidation ratio
PVD	Prefabricated Vertical Drains
RMSE	Root Mean Square Error
SWCC	Soil Water Characteristic Curves
VMD	Vietnamese Mekong Delta

CRediT authorship contribution statement

Felix Dörr: Writing – original draft, Validation, Methodology, Investigation, Formal analysis, Data curation, Conceptualization. **Jonas Bauer:** Writing – review & editing, Investigation, Formal analysis. **Tran Viet Hoan:** Writing – review & editing, Investigation, Data curation. **Le Thi Mai Van:** Writing – review & editing, Project administration, Data curation. **Andreas Schenk:** Writing – review & editing, Data curation. **Nils Dörr:** Writing – review & editing, Methodology, Formal analysis. **Franz Nestmann:** Writing – review & editing, Supervision, Resources, Project administration, Funding acquisition. **Stefan Norra:** Writing – review & editing, Supervision, Resources, Project administration, Funding acquisition.

Declaration of Generative AI and AI-assisted technologies in the writing process

During the preparation of this work the author(s) used ChatGPT in order to improve language and readability of the manuscript text. After using this tool/service, the authors reviewed and edited the content as needed and take full responsibility for the content of the published article.

Declaration of competing interest

The authors declare that they have no known competing financial interests or personal relationships that could have appeared to influence the work reported in this paper.

Acknowledgements

This research was conducted in the frame of the project “ViWaT – Vietnam Water Technologies” funded by the German Federal Ministry of Research, Technology and Space (funding reference: 02WCL1474A). Felix Dörr thanks the Hector Fellow Academy for support. We gratefully thank the Vietnamese Ministry of Science and Technology (MOST), the

National Center for Water Resources Planning and Investigation (NAWAPI) and the Department of Natural Resources and Environment Ca Mau (DONRE Ca Mau) for the good cooperation and providing data. We thank the KIT Institute of Soil Mechanics and Rock Mechanics (KIT-IBF) for providing access to the geotechnical laboratory facilities, and Hauke Sattler of the Institute of Environmental Sciences and Geography, Soil Sciences and Geoecology at the University of Potsdam for determining the soil-water characteristic curves. We acknowledge support by the KIT-Publication Fund of the Karlsruhe Institute of Technology, Germany.

Appendix A. Supplementary data

Supplementary data to this article can be found online at https://doi.org/10.1016/j.scitotenv.2026.181850.

Data availability

Data will be made available on request.

References

Allen, D.R., Mayuga, M.N., 1970. The Mechanics of Compaction and Rebound. International Hydrological Decade, Symposium on Land Subsidence, Tokyo, Japan 17–22 Sept. Wilmington Oil Field, Long Beach, California, USA.

Anderson, H.R., 1978. Hydrogeologic Reconnaissance of the Mekong Delta in South Vietnam and Cambodia. Contributions to The Hydrology of Asia and Oceania, Geological Survey Water-Supply Paper 1608-R.

Baldan, S., Minderhoud, P.S.J., Xotta, R., Zoccarato, C., Teatini, P., 2025. Data-driven 3D modelling of long-term Holocene delta evolution and sediment compaction: the Mekong Delta. Earth Surf. Process. Landf. 50. https://doi.org/10.1002/esp.6046.

Baú, D., Ferronato, M., Gambolati, G., Teatini, P., 2004. Surface flow boundary conditions in modeling land subsidence due to fluid withdrawal. Groundwater 42, 516–525. https://doi.org/10.1111/j.1745-6584.2004.tb02620.x.

Boone, S.J., 2010. A critical reappraisal of "preconsolidation pressure" interpretations using the oedometer test. Can. Geotech. J. 47, 281–296. https://doi.org/10.1139/T09-093.

Buffardi, C., Minderhoud, P.S.J., Mandolini, A., Ruberti, D., 2025. Characterizing Holocene sediments for assessing coastal-deltaic subsidence: the role of cone penetration tests and geomechanics. Front. Earth Sci. 13. https://doi.org/10.3389/feart.2025.1585388.

Danh, V.T., Khai, H.V., 2015. Household demand and supply for clean groundwater in the Mekong Delta, Vietnam. Renew. Wind Water Sol. 2, 4. https://doi.org/10.1186/s40807-014-0004-7.

Davydzenka, T., Tahmasebi, P., Shokri, N., 2024. Unveiling the global extent of land subsidence: the sinking crisis. Geophys. Res. Lett. 51. https://doi.org/10.1029/2023gl104497.

De Wit, K., Lexmond, B.R., Stouthamer, E., Neussner, O., Dörr, N., Schenk, A., Minderhoud, P.S.J., 2021. Identifying causes of urban differential subsidence in the Vietnamese Mekong Delta by combining InSAR and field observations. Remote Sens. 13, 189. https://doi.org/10.3390/rs13020189.

Domenico, P.A., Schwartz, F.W., 1998. Physical and Chemical Hydrogeology, 2. Ed., paperback. ed. Wiley, New York Chichester Weinheim.

Dörr, N., Schenk, A., Hinz, S., 2024. Land subsidence in the Mekong Delta derived from advanced persistent scatterer interferometry with an infrastructural reference network. IEEE J. Sel. Top. Appl. Earth Obs. Remote Sens. 17, 12077–12091. https://doi.org/10.1109/jstars.2024.3420130.

Dörr, F., Bauer, J., Rau, G.C., Lewi, E., Hoan, V.T., Van, L.T.M., Valois, R., Steinel, A., Nestmann, F., Norra, S., 2026. The recharge illusion: how seasonal surface loading can hide continuing groundwater resource declines in confined deltaic aquifers. J. Hydrol. 665, 134674. https://doi.org/10.1016/j.jhydrol.2025.134674.

Duy, N.L., Nguyen, T.V.K., Nguyen, D.V., Tran, A.T., Nguyen, H.T., Heidbüchel, I., Merz, B., Apel, H., 2021. Groundwater dynamics in the Vietnamese Mekong Delta: trends, memory effects, and response times. J. Hydrol. Reg. Stud. 33, 100746. https://doi.org/10.1016/j.ejrh.2020.100746.

Erban, L.E., Gorelick, S.M., Zebker, H.A., 2014. Groundwater extraction, land subsidence, and sea-level rise in the Mekong Delta, Vietnam. Environ. Res. Lett. 9, 084010. https://doi.org/10.1088/1748-9326/9/8/084010.

Feng, W.-Q., Zheng, X.-C., Yin, J.-H., Chen, W.-B., Tan, D.-Y., 2019. Case study on long-term ground settlement of reclamation project on clay deposits in Nansha of China. Mar. Georesour. Geotechnol. 39, 372–387. https://doi.org/10.1080/1064119X.2019.1704319.

Galavi, V., 2010. Groundwater Flow, Fully Coupled Flow Deformation and Undrained Analyses in PLAXIS 2D and 3D. Plaxis, Delft Neth.

Gambolati, G., Teatini, P., 2021. Land Subsidence and its Mitigation. The Groundwater Project. https://doi.org/10.21083/978-1-77470-001-3.

Gambolati, G., Teatini, P., Baú, D., Ferronato, M., 2000. Importance of poroelastic coupling in dynamically active aquifers of the Po River Basin, Italy. Water Resour. Res. 36, 2443–2459. https://doi.org/10.1029/2000WR900127.

Giao, P.H., Dung, N.T., Long, P.V., 2008. An integrated geotechnical–geophysical investigation of soft clay at a coastal site in the Mekong Delta for oil and gas infrastructure development. Can. Geotech. J. 45, 1514–1524. https://doi.org/10.1139/t08-077.

Hoan, T.V., Richter, K.-G., Börsig, N., Bauer, J., Ha, N.T., Norra, S., 2022. An improved groundwater model framework for aquifer structures of the quaternary-formed sediment body in the southernmost parts of the Mekong Delta, Vietnam. Hydrology 9, 61. https://doi.org/10.3390/hydrology9040061.

Hoan, T.V., Richter, K.-G., Dörr, F., Bauer, J., Börsig, N., Steinel, A., Le, V.T.M., Pham, V. C., Than, D.V., Norra, S., 2025. The utilization of a 3D groundwater flow and transport model for a qualitative investigation of groundwater salinization in the Ca Mau Peninsula (Mekong Delta, Vietnam). Hydrology 12, 126. https://doi.org/10.3390/hydrology12050126.

Holzer, T.L., Johnson, A.I., 1985. Land subsidence caused by ground water withdrawal in urban areas. GeoJournal 11. https://doi.org/10.1007/BF00186338.

Kooi, H., Erkens, G., 2020. Creep consolidation in land subsidence modelling; integrating geotechnical and hydrological approaches in a new MODFLOW package (SUB-CR). Proc. IAHS 382, 499–503. https://doi.org/10.5194/piahs-382-499-2020.

Le, H.-A., Nguyen, T., Gratiot, N., Deleersnijder, E., Soarez-Frazao, S., 2023. The multi-channel system of the Vietnamese Mekong Delta: impacts on the flow dynamics under relative sea-level rise scenarios. Water 15 (20), 3597. https://doi.org/10.3390/w15203597.

Lee, I., Choi, Y.-T., Lee, M., Yune, C.-Y., 2018. Effect of groundwater level variation on residual settlement of Korean high-speed railway on soft ground. KSCE J. Civ. Eng. 22, 3312–3320. https://doi.org/10.1007/s12205-017-0472-6.

Lexmon, B.R., Guzy, A., Torfs, P.J.J.F., Pham, H.V., Essink, G.H.P.O., Teatini, P., Stouthamer, E., Minderhoud, P.S.J., 2025. Simulating Extraction-induced Subsidence in the Mekong Delta: Investigating the Effects of Discretization and Conductivity Uncertainty. https://doi.org/10.21203/rs.3.rs-7609506/v1.

Logan, W.S., 2002. Vietnam's highway no. 1: corridor of power and patrimony. Hist. Environ. 23–27.

Mi, N.V.A., Thongchart, S., Mairaing, W., 2023. Roadway settlement characteristics on Mekong Delta for various landforms. Int. J. GEOMATE 25. https://doi.org/10.21660/2023.111.4006.

Minderhoud, P.S.J., Erkens, G., Pham, V.H., Bui, V.T., Erban, L., Kooi, H., Stouthamer, E., 2017. Impacts of 25 years of groundwater extraction on subsidence in the Mekong Delta, Vietnam. Environ. Res. Lett. 12, 064006. https://doi.org/10.1088/1748-9326/aa7146.

Minderhoud, P.S.J., Coumou, L., Erban, L.E., Middelkoop, H., Stouthamer, E., Addink, E. A., 2018. The relation between land use and subsidence in the Vietnamese Mekong delta. Sci. Total Environ. 634, 715–726. https://doi.org/10.1016/j.scitotenv.2018.03.372.

Minderhoud, P.S.J., Coumou, L., Erkens, G., Middelkoop, H., Stouthamer, E., 2019. Mekong delta much lower than previously assumed in sea-level rise impact assessments. Nat. Commun. 10, 1–13. https://doi.org/10.1038/s41467-019-116021.

Minderhoud, P.S.J., Middelkoop, H., Erkens, G., Stouthamer, E., 2020. Groundwater extraction may drown mega-delta: projections of extraction-induced subsidence and elevation of the Mekong delta for the 21st century. Environ. Res. Commun. 2, 011005. https://doi.org/10.1088/2515-7620/ab5e21.

Montoya-Araque, E.A., Aparicio-Ortube, A.J., Zapata-Medina, D.G., Arboleda-Monsalve, L.G., 2022. An open-source application software to determine the preconsolidation pressure of soils in incremental loading oedometer testing: pySigmaP. SoftwareX 17, 100990. https://doi.org/10.1016/j.softx.2022.100990.

Nguyen Thi, N., Son, B.T., Ngoc, D.M., 2020. Research on horizontal coefficient of consolidation of Vietnam's soft soil. J. Eng. 2020, 1–13. https://doi.org/10.1155/2020/3697689.

Osenbrück, K., Steinel, A., Montcoudiol, N., Manh, L.V., Bäumle, R., 2025. Geochemical evolution and flow of groundwater impacted by long-term abstraction in the Mekong Delta, Vietnam. J. Hydrol. 655, 132881. https://doi.org/10.1016/j.jhydrol.2025.132881.

Qi, J., Xie, Y., Li, C., Guo, H., Wang, Y., 2025. Creep behavior of clayey soil and its model prediction in the Cangzhou land subsidence area. Sci. Rep. 15, 9130. https://doi.org/10.1038/s41598-025-93928-z.

Syvitski, J.P.M., Kettner, A.J., Overeem, I., Hutton, E.W.H., Hannon, M.T., Brakenridge, G.R., Day, J., Vörösmarty, C., Saito, Y., Giosan, L., Nicholls, R.J., 2009. Sinking deltas due to human activities. Nat. Geosci. 2, 681–686. https://doi.org/10.1038/ngeo629.

Tavenas, F., Jean, P., Leblond, P., Leroueil, S., 1983. The permeability of natural soft clays. Part II: permeability characteristics. Can. Geotech. J. 20, 645–660. https://doi.org/10.1139/t83-073.

Tuller, M., Or, D., 2005. Water retention and characteristic curve. In: Encyclopedia of Soils in the Environment. Elsevier, pp. 278–289. https://doi.org/10.1016/B0-12-348530-4/00376-3.

Van, L.T.T., Lertsirivorakul, R., Vuong, B.T., Thang, C.H., 2023. Groundwater recharge in Mekong River Delta: An application of the water-table fluctuation method in the Long Xuyen quadrangle and the Ca Mau peninsula. Songklanakarin J. Sci. Technol. 45.

Vermeer, P.A., Neher, H.P., 1999. A soft soil model that accounts for creep. In: Brinkgreve, R.B.J. (Ed.), Beyond 2000 in Computational Geotechnics. Routledge, pp. 249–261. https://doi.org/10.1201/9781315138206-24.

Wagner, F., Tran, V.B., Renaud, F.G., 2012. Chapter 7, groundwater resources in the Mekong Delta: availability, utilization and risks. In: Renaud .K.C., Fabrice G. (Ed.), The Mekong Delta System - Interdisciplinary Analysis of a River Delta, 1st ed. Springer, Dordrecht, pp. 201–220. https://doi.org/10.1007/978-94-007-3962-8_7.

Xu, J., Jitteh, K., Li, Y., Chen, J., 2025. Predictive model for estimating the weight of existing RC buildings using easily accessible structural parameters. Struct. Control. Health Monit. 2025, 6558932. https://doi.org/10.1155/stc/6558932.
Yuill, B., Lavoie, D., Reed, D.J., 2009. Understanding subsidence processes in coastal Louisiana. J. Coast. Res. 10054, 23–36. https://doi.org/10.2112/SI54-012.1.
Zoccarato, C., Minderhoud, P.S.J., Teatini, P., 2018. The role of sedimentation and natural compaction in a prograding delta: insights from the mega Mekong Delta, Vietnam. Sci. Rep. 8, 11437. https://doi.org/10.1038/s41598-018-29734-7.